

## Journal Pre-proof

Implementation and evaluation of a three-level grid method for CFD-DEM simulations of dense gas-solid flows

Daniel Hirche, Olaf Hinrichsen

PII: S2666-8211(20)30048-X  
DOI: <https://doi.org/10.1016/j.cej.2020.100048>  
Reference: CEJA 100048



To appear in: *Chemical Engineering Journal Advances*

Received date: 4 September 2020  
Revised date: 30 October 2020  
Accepted date: 2 November 2020

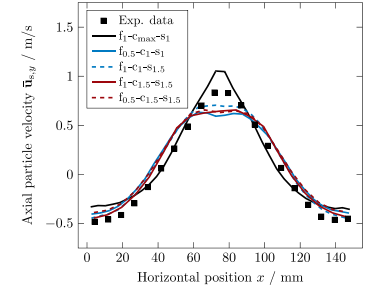
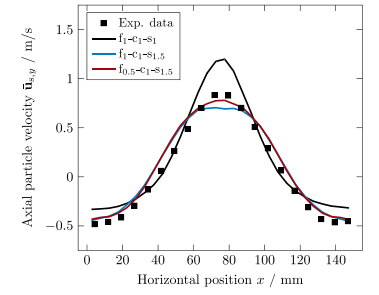
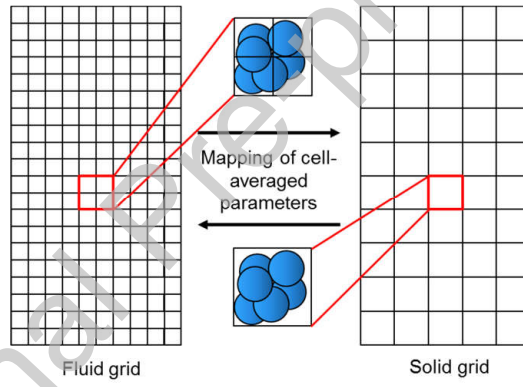
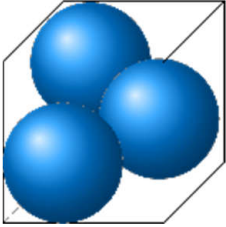
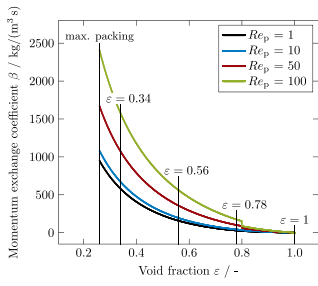
Please cite this article as: Daniel Hirche, Olaf Hinrichsen, Implementation and evaluation of a three-level grid method for CFD-DEM simulations of dense gas-solid flows, *Chemical Engineering Journal Advances* (2020), doi: <https://doi.org/10.1016/j.cej.2020.100048>

This is a PDF file of an article that has undergone enhancements after acceptance, such as the addition of a cover page and metadata, and formatting for readability, but it is not yet the definitive version of record. This version will undergo additional copyediting, typesetting and review before it is published in its final form, but we are providing this version to give early visibility of the article. Please note that, during the production process, errors may be discovered which could affect the content, and all legal disclaimers that apply to the journal pertain.

© 2020 Published by Elsevier B.V.  
This is an open access article under the CC BY-NC-ND license  
(<http://creativecommons.org/licenses/by-nc-nd/4.0/>)

**Highlights**

- Fundamental Development of a novel three-level grid CFD-DEM simulation in OpenFOAM®.
- Evaluation of a single-, dual-grid and the newly developed three-level grid method.
- Validation with a pseudo 2D and 3D fluidized bed from literature.
- Combination of a multi-level grid approach with the coarse grain method.



# Implementation and evaluation of a three-level grid method for CFD-DEM simulations of dense gas-solid flows

Daniel Hirche<sup>a,b</sup>, Olaf Hinrichsen<sup>a,b,\*</sup>

<sup>a</sup>*Department of Chemistry, Technical University of Munich, Lichtenbergstr. 4, D-85748 Garching near Munich, Germany*

<sup>b</sup>*Catalysis Research Center, Technical University of Munich, Ernst-Otto-Fischer-Str. 1, D-85748 Garching near Munich, Germany*

---

## Abstract

The use CFD-DEM for the simulation of dense gas-solid flows comes with limitations based on the numerical cell size depending on the diameter of the particles. With the introduction of a multi-grid approach, i.e., the calculation of the fluid phase and the solid phase are done with two separate meshes, a finer and a coarser one, this limitation can be overcome. In this work, a three-level grid approach is proposed, in which an additional numerical grid is used to transform parameters used for the solid-fluid momentum exchange from the Lagrangian to the Eulerian grid. The resolution of this newly introduced grid lies in between the resolution of the two other meshes. A conventional single- and dual-grid, as well as the newly introduced three-level grid approach were validated with experimental data in literature and afterwards compared in terms of accuracy and simulation speed. A multi-grid approach, dual- or three-level, shows a higher accuracy than the single-grid method. An additional third grid achieves in almost all cases slightly better results than the dual-grid method while the increase in simulation time is negligible. A coarsening of the solid grid has a higher effect on accuracy than the refinement of the fluid grid. Furthermore, the coarse grain method was implemented to increase simulation speed. Still, the three-level grid approach requires a deeper understanding in the resolution of the numerical grid as there are more degrees

of freedom for the cell sizes, but an adequate choice of the numerical grid can drastically improve the simulation accuracy and speed in combination with a coarse grain method.

**Keywords:** CFD-DEM, fluidized bed, multi-grid, void fraction, coarse grain

---

## 1. Introduction

Computational Fluid Dynamics (CFD) as a simulation approach for modeling gas-solid flows, in particular, fluidized bed [1], has been proven to be accurate in predicting the hydrodynamics, thermodynamics and chemical reactions of the system [2–7]. Several approaches exist to model gas-solid flows and the most common ones are the Lattice-Boltzmann method (LBM), Discrete Element Method [8] coupled with CFD (CFD-DEM) [9, 10] and the Two-Fluid model (TFM) [11, 12]. While the LBM is mostly used for the investigation of small-scale systems to derive correlations used for more abstract models [13], CFD-DEM found its use in the simulation of small- to medium-scale systems with mostly larger particles [14–16], e.g., group D particles according to the Geldart classification [17]. Due to the Eulerian character in the TFM, it is used for large-scale systems [18, 19], independent of the particle size. Using CFD-DEM the particles are calculated in a Lagrangian way using DEM and the fluid flow is modeled as a continuum in a Eulerian way. In order to couple the phases, crucial parameters from both phases have to be transformed from a Lagrangian parameter to a Eulerian one and vice versa, e.g., the number of particles (Lagrangian parameter) has to be transformed to a Eulerian parameter, the void fraction. There exist certain restrictions for the applicability of CFD-DEM simulations. One of the major restrictions when using CFD-DEM is the relatively long simulation time compared to the TFM approach when simulating

---

\*Corresponding author

Email address: olaf.hinrichsen@ch.tum.de (Olaf Hinrichsen)

a high amount of particles [20]. Especially for particles with a small diameter, e.g., Geldart group B particles, the use of CFD-DEM might not be feasible in terms of simulation time. A method to increase the simulation speed for CFD-DEM simulations is the so called coarse grain (CG) method developed by Sakai and Koshizuka [21]. Here, a group of particles are lumped together to a cluster of particles forming a bigger parcel [22]. The CG method was applied for multiple geometry scales in literature, e.g., for dense medium cyclones [23]. Mass and energy conservation in this method is ensured with an introduced scaling factor. A higher scaling factor results in more particles being lumped together to a bigger parcel, hence less particles need to be simulated and the simulation speed increases. Therefore, the level of the scaling factor is limited by applicability and resulting accuracy. Takabatake et al. [24] used a scaling factor of up to three for a gas-solid spouted bed and validated their simulations with experiments. They achieved reasonable results regarding the mixing state. Even higher scaling factors were applied for the simulation of fluidized beds, e.g. a scaling factor of up to eight [25]. The CG method was also applied for the simulation of a 3 m high circulating fluidized bed reactor [26] and even larger scales with Geldart group B particles with a scaling factor of approximately 60 [27]. The higher the scaling factor, the larger the size of the particle cluster. The size of the particles can be another major problem regarding dense solid flow simulations using CFD-DEM. Peng et al. [28] proposed a cell-to-particle diameter ratio of at least 3.82 to get accurate simulation results. But bigger cells result in a worse resolution due to the coarser numerical grid size. Hence, the choice of an adequate numerical grid size is crucial. The calculations for the Lagrangian particle tracking, i.e., the particle movement, is at first sight independent of the numerical grid. Using the finite volume method, the fluid phase is calculated on a numerical grid consisting of 3D cells. The coupling between the particles and

the fluid phase is done by transforming Lagrangian to Eulerian parameters, e.g., the velocities of particles residing in a specific cell are averaged to obtain a cell-averaged value used for the fluid phase calculations. Alobaid et al. [29] proposed a dual-grid method, splitting a single numerical grid in two separate grids: a finer grid used for the calculation of the fluid phase and a coarser grid for the Lagrangian particle tracking. The implementation of a multi-grid method for CFD-DEM simulations can have multiple benefits. The major advantages are the increasing accuracy of the results, the higher resolution of the obtained data and the representation of complex or narrow geometries. With a dual-grid approach the numerical grid gets independent of the particle size, but a mapping of crucial properties between the two numerical grids becomes necessary, where a conservative interpolation method with second-order accuracy showed the best results [30]. The dual-grid approach was applied and validated in several cases, e.g., spouted fluidized beds [31] or jetting fluidized beds [32].

In the following, a three-level grid approach is proposed, extending the conventional dual-grid approach by another numerical grid for the calculation and determination of specific Eulerian parameters from Lagrangian ones. Farzaneh et al. [33] proposed a three-level grid approach, but in their work they used one grid for the fluid phase and two grids for two different sized particle phases. In our work, one grid is used for the Lagrangian particle tracking independent of the particle size. It is shown in detail how a multi-grid method consisting of two and three numerical grids can result into the aforementioned advantages. Experimental data from literature is used to validate the multi-grid method and it will be compared to a conventional CFD-DEM solver. Lastly, the additional time needed for the mapping due to the third numerical grid will be evaluated.

## 2. Methodology

First, the numerical methods for CFD-DEM are presented and in the second part the necessity and advantages of a multi-level grid method, as well as, the solving procedures will be discussed in detail.

### 2.1. Numerical Methods

The calculation of the fluid motion is based on the continuity equation (cf. Equation 1) and the momentum balance based on the volume-averaged Navier-Stokes equations (cf. Equation 2):

$$\frac{\partial \varepsilon}{\partial t} + \nabla \cdot (\varepsilon \mathbf{u}_f) = 0 \quad (1)$$

and

$$\frac{\partial (\varepsilon \rho_f \mathbf{u}_f)}{\partial t} + \nabla \cdot (\varepsilon \rho_f \mathbf{u}_f \mathbf{u}_f) = -\varepsilon \nabla p + \varepsilon \rho_f \mathbf{g} + \nabla \cdot (\varepsilon \bar{\bar{\tau}}_f) + \mathbf{M}_{f,s}. \quad (2)$$

Here,  $\mathbf{u}_f$  represents the velocity,  $\rho_f$  the density and  $\varepsilon$  the volume fraction of the fluid phase.

The calculation of the cell-averaged volumetric fraction of the fluid phase  $\varepsilon$  in CFD-DEM simulation is dependent on the number of particles residing in the considered cell. There exist several different methods for the determination of the volumetric volume fraction, e.g., analytical, porous cube model [14] or diffusion-based models [34, 35]. In the following simulations the calculation of the volume fraction is done via the Particle Centroid Method (PCM). According to the PCM the volume of all particles residing in the considered cell  $\sum_{p \in \text{cell}} V_p$  accounts for the



calculation of the volume fraction of the specific phase:

$$\varepsilon = 1 - \frac{1}{V_{\text{cell}}} \sum_{\forall p \in \text{cell}} V_p. \quad (3)$$

The stress tensor of the fluid phase  $\bar{\bar{\tau}}_f$  is given by Enwald et al. [11]:

$$\bar{\bar{\tau}}_f = \eta_{\text{shear}} \left[ \nabla \mathbf{u}_f + (\nabla \mathbf{u}_f)^T \right] - \left( \eta_{\text{bulk}} - \frac{2}{3} \eta_{\text{shear}} \right) (\nabla \cdot \mathbf{u}_f) \bar{\bar{\mathbf{I}}}. \quad (4)$$

The momentum exchange  $\mathbf{M}_{f,s}$  accounts for the coupling forces between the fluid and the solid phase. In the later numerical implementation,  $\mathbf{M}_{f,s}$  is split up into an explicit and an implicit term due to stability reasons:

$$\mathbf{M}_{f,s} = \frac{\sum \mathbf{F}_{f,p}}{V_{\text{cell}} |\mathbf{u}_f - \mathbf{u}_s|} \cdot \mathbf{u}_f - \frac{\sum \mathbf{F}_{f,p}}{V_{\text{cell}} |\mathbf{u}_f - \mathbf{u}_s|} \cdot \mathbf{u}_s, \quad (5)$$

with the cell-averaged velocity of the particulate phase  $\mathbf{u}_s$  and the coupling forces between the fluid and the particle  $\mathbf{F}_{f,p}$ . The cell-averaged velocity of the solid phase  $\mathbf{u}_s$  is determined in accordance to the PCM with the individual velocities of the tracked particles  $\mathbf{u}_p$  and the total number of particles residing in the considered cell  $n_p$ :

$$\mathbf{u}_s = \frac{1}{n_p} \sum_{\forall p \in \text{cell}} \mathbf{u}_p. \quad (6)$$

The coupling forces between the fluid and solid phases consist of the drag, buoyancy and lift force, among others. According to Papadikis et al. [36] the drag force  $\mathbf{F}_d$  was determined as the major parameter for the fluid-particle force coupling. It can be calculated with the momentum exchange coefficient  $\beta$ , the relative velocity of the fluid phase and the individual particle  $(\mathbf{u}_f - \mathbf{u}_p)$ ,

the mass of the particle  $m_p$  and the corresponding density  $\rho_p$  according to

$$\mathbf{F}_d = \beta (\mathbf{u}_f - \mathbf{u}_p) \frac{m_p}{\rho_p}. \quad (7)$$

The determination of the momentum exchange coefficient  $\beta$  can be done according to different models. One of the most used models is the Gidaspow model [37, 38] which is a combination of the Ergun correlation [39] for dense gas-solid flows and the correlation from Wen and Yu [40] for dilute ones:

$$\beta = \begin{cases} 150 \frac{(1-\varepsilon)^2 \eta}{\varepsilon d_p^2} + 1.75 (1-\varepsilon) \frac{\rho_f}{d_p} |\mathbf{u}_f - \mathbf{u}_p|, & \varepsilon < 0.8 \\ \frac{3}{4} C_d \frac{\varepsilon (1-\varepsilon)}{d_p} \rho_f |\mathbf{u}_f - \mathbf{u}_p| \varepsilon^{-2.65}, & \varepsilon \geq 0.8. \end{cases} \quad (8)$$

The drag coefficient  $C_d$  is dependent on the particle Reynolds number  $Re_p$ :

$$C_d = \begin{cases} \frac{24}{Re_p} (1.0 + 0.15 Re_p^{0.687}), & Re_p \leq 1000 \\ 0.44, & Re_p > 1000 \end{cases} \quad (9)$$

and

$$Re_p = \frac{\varepsilon d_p |\mathbf{u}_f - \mathbf{u}_p| \rho_f}{\eta}. \quad (10)$$

Benyahia et al. [41] extended the Hill-Koch-Ladd (HKL) drag correlation [42, 43] from Lattice-Boltzmann simulations to a wider range of void fractions and particle Reynolds numbers, the so called extended HKL drag-model, which is another widely used equation for the calculation of the

momentum exchange coefficient:

$$\beta = \frac{3}{4} \frac{C_d \alpha (1 - \alpha) \rho_f |\mathbf{u}_f - \mathbf{u}_p|}{d_p} \quad (11)$$

with the drag coefficient

$$C_d = 12 \frac{(1 - \alpha)^2}{Re_p^*} F. \quad (12)$$

The dimensionless drag force  $F$  is dependent on the degree of turbulence with the adjusted Reynolds number  $Re_p^*$  and the solid volume fraction  $\alpha$  with  $\alpha = 1 - \varepsilon$ :

$$F = 1 + 3/8 Re_p^* \quad \text{for } \alpha \leq 0.01 \text{ and } Re_p^* \leq \frac{F_2 - 1}{3/8 - F_3} \quad (13)$$

$$F = F_0 + F_1 Re_p^{*2} \quad \text{for } \alpha > 0.01 \text{ and } Re_p^* \leq \frac{F_3 + \sqrt{F_3^2 - 4F_1(F_0 - F_2)}}{2F_1} \quad (14)$$

$$F = F_2 + F_3 Re_p^* \quad \text{otherwise,} \quad (15)$$

with

$$Re_p^* = \frac{1}{2} Re_p. \quad (16)$$

The separate contributions for the inertial coefficients  $F_0$ ,  $F_1$ ,  $F_2$  and  $F_3$  are determined by

$$F_0 = \begin{cases} (1-w) \left[ \frac{1+3\sqrt{\frac{\alpha}{2}} + \frac{135}{64}\alpha \ln(\alpha) + 17.14\alpha}{1+0.681\alpha-8.48\alpha^2+8.16\alpha^3} \right] + w \left[ 10 \frac{\alpha}{(1-\alpha)^3} \right] & \text{for } 0.01 < \alpha < 0.4 \\ 10 \frac{\alpha}{(1-\alpha)^3} & \text{for } \alpha \geq 0.4 \end{cases} \quad (17)$$

$$F_1 = \begin{cases} \frac{\sqrt{\frac{\alpha}{2}}}{40} & \text{for } 0.01 < \alpha \leq 0.1 \\ 0.11 + 0.00051 \exp(11.6\alpha) & \text{for } \alpha > 0.1 \end{cases} \quad (18)$$

$$F_2 = \begin{cases} (1-w) \left[ \frac{1+3\sqrt{\frac{\alpha}{2}} + \frac{135}{64}\alpha \ln(\alpha) + 17.89\alpha}{1+0.681\alpha-11.03\alpha_s^2+15.41\alpha_s^3} \right] + w \left[ 10 \frac{\alpha}{(1-\alpha)^3} \right] & \text{for } 0.01 < \alpha < 0.4 \\ 10 \frac{\alpha}{(1-\alpha)^3} & \text{for } \alpha \geq 0.4 \end{cases} \quad (19)$$

$$F_3 = \begin{cases} 0.9351\alpha + 0.03667 & \text{for } 0.01 < \alpha < 0.0953 \\ 0.0673 + 0.212\alpha + 0.0232/(1-\alpha)^5 & \text{for } \alpha \geq 0.0953 \end{cases} \quad (20)$$

with

$$w = \exp(-10(0.4 - \alpha)/\alpha). \quad (21)$$

The movement of the particles according to a Lagrangian way is done with the use of Newton's second law of motion with a force (cf. Equation 22) and torque balance (cf. Equation 23).

$$m_p \frac{d\mathbf{u}_p}{dt} = \sum \mathbf{F}_p. \quad (22)$$

The torque of the particle  $\mathbf{T}_p$  is calculated with the moment of inertia  $I_p$  and the time derivative

of the angular velocity  $\omega_p$ :

$$I_p \frac{d\omega_p}{dt} = \mathbf{T}_p. \quad (23)$$

The forces acting on the considered particle  $\sum \mathbf{F}_p$  consist of contact forces  $\mathbf{F}^c$  including collisions, non-contact forces  $\mathbf{F}^{nc}$  including forces due to gravity and particle-fluid interaction forces  $\mathbf{F}_{f,p}$ , i.e., drag force  $\mathbf{F}_d$  (cf. (7)), pressure gradient force  $\mathbf{F}_{\nabla p}$ , gravity force  $\mathbf{F}_g$  and buoyancy force  $\mathbf{F}_b$ :

$$\mathbf{F}_{\nabla p} = V_p \nabla p \quad (24)$$

and

$$\mathbf{F}_g - \mathbf{F}_b = V_p (\rho_p - \rho_f) \mathbf{g}. \quad (25)$$

The contact force  $\mathbf{F}^c$  can result from particle-particle collisions,  $\mathbf{F}_p^c$ , or from particle-wall collisions,  $\mathbf{F}_w^c$ . Several models were proposed in literature for the force-displacement [44], most of them differentiated by linear and non-linear spring and damping models [45]. In this work, the non-linear model based on the Hertzian theory is used. Each of the above stated forces is divided according to the soft-sphere and spring, slider and dash-pot model into a normal and tangential contact force:

$$\mathbf{F}^c = \mathbf{F}_n^c + \mathbf{F}_t^c \quad (26)$$

with the normal contact force  $\mathbf{F}_n^c$  and tangential contact force  $\mathbf{F}_t^c$ , respectively. According

to the Hertzian spring-theory and the consideration of damping, the normal contact force can be calculated with

$$\mathbf{F}_n^c = -k_n \Delta x_{n,ol}^b \mathbf{n} - \eta_n \mathbf{u}_{n,rel}. \quad (27)$$

The normal spring stiffness is defined as  $k_n$ , the overlap between the two colliding particles is  $\Delta x_{n,ol}$ , the exponent  $b$  for the Hertzian spring theory has a value of 1.5,  $\mathbf{n}$  represents the unity vector in normal direction, the damping coefficient for the normal force is  $\eta_n$  and  $\mathbf{u}_{n,rel}$  defines the relative velocity of the two colliding particles in normal direction of the collision. The normal spring stiffness  $k_n$  is dependent on the effective radius  $r_{eff}$ , the Young's modulus  $E$  and the Poisson ratio  $\nu$ :

$$k_n = \frac{4}{3} \sqrt{r_{eff}} \frac{E}{2(1-\nu^2)}. \quad (28)$$

The effective radius can be calculated with the two diameters of the colliding particles  $d_1$  and  $d_2$ :

$$r_{eff} = 0.5 \frac{d_1 d_2}{d_1 + d_2}. \quad (29)$$

For uniform particles of the same size, i.e.,  $d_1 = d_2$ , the effective radius becomes  $r_{eff} = 0.25d_p$  and Equation 28 can be simplified to

$$k_n = \frac{1}{3} \sqrt{d_p} \frac{E}{1-\nu^2}. \quad (30)$$

The damping coefficient for the normal contact force  $\eta_n$  is calculated according to the heuristically equation by Tsuji et al. [9]:

$$\eta_n = \alpha_n \sqrt{M_{\text{red}} k_n} \Delta x_{\text{ol}}^{0.25} \quad (31)$$

with the reduced mass of the two colliding particles  $M_{\text{red}}$

$$M_{\text{red}} = \frac{m_1 m_2}{m_1 + m_2} \quad (32)$$

and for uniform particles in terms of size and density

$$M_{\text{red}} = 0.5 m_p. \quad (33)$$

Equation 31 then simplifies to

$$\eta_n = \alpha_n \sqrt{0.5 m_p k_n} \Delta x_{\text{ol}}^{0.25}. \quad (34)$$

The parameter  $\alpha_n$  is an empirical parameter and is related to the coefficient of restitution  $e_n$  [9, 46] according to:

$$\alpha_n = \begin{cases} \frac{-2 \ln e_n}{\sqrt{\pi^2 + \ln^2 e_n}} & \text{if } 0 < e_n \leq 0.8 \\ 2 & \text{if } e_n = 0. \end{cases} \quad (35)$$

The tangential component of the contact force  $\mathbf{F}_t^c$  can be calculated with the tangential spring stiffness  $k_t$ , the tangential overlap  $\Delta x_{\text{ol}, t}$ , the unit vector in tangential direction  $\mathbf{t}$ , the tangential

damping coefficient  $\eta_t$  and the tangential slip velocity  $\mathbf{u}_{t, \text{slip}}$ :

$$\mathbf{F}_t^c = -k_t \Delta x_{ol, t} \mathbf{t} - \eta_t \mathbf{u}_{t, \text{slip}}. \quad (36)$$

Furthermore, according to the Coulomb friction law, sliding can occur if the tangential component of the contact exceeds the Coulomb friction force  $\mu_f |\mathbf{F}_n^c|$ , with  $\mu_f$  being the friction coefficient.

The tangential component of the contact force therefore follows the equation:

$$\mathbf{F}_t^c = \min(-k_t \Delta x_{ol, t} \mathbf{t} - \eta_t \mathbf{u}_{t, \text{slip}}, -\mu_f |\mathbf{F}_n^c| \mathbf{t}). \quad (37)$$

A popular method to increase the speed of CFD-DEM simulations is the coarse grain (CG) model proposed by Sakai and Koshizuka [21]. Here, several smaller particles are represented by one larger particle. A coarse grain factor  $f_{CG}$  is introduced describing the ratio of the diameter of the larger coarse grain particle to the original smaller particle  $d_{p, CG}/d_p$ , therefore, the particle diameter of the larger coarse grain particle can be calculated with:

$$d_{p, CG} = f_{CG} d_p. \quad (38)$$

The total number of new coarse grain particles is decreased by a value of  $f_{CG}^3$ . The simulation time decreases as well, if the DEM-calculation is the speed determining step, as the number of Lagrangian equations decreases. With the assumption of the CG model that all small particles of a parcel shall resemble and evince the same physical properties and fluid dynamic behavior, several modifications for the Lagrangian equations need to be made to assure the same magnitude of forces. The forces acting on the coarse grain particle cluster, i.e., the drag force  $\mathbf{F}_{d, CG}$ , gravity



force  $\mathbf{F}_{g, CG}$  and buoyancy force  $\mathbf{F}_{b, CG}$  are scaled with the coarse grain factor  $f_{CG}$  accordingly:

$$\mathbf{F}_{d, CG} = f_{CG}^3 \mathbf{F}_{d, orig} \quad (39)$$

$$\mathbf{F}_{g, CG} = f_{CG}^3 \mathbf{F}_{g, orig} \quad (40)$$

$$\mathbf{F}_{b, CG} = f_{CG}^3 \mathbf{F}_{b, orig}. \quad (41)$$

It is further assumed that the velocity of the coarse grained particle cluster is equal to the average velocity of the smaller particles, as well as a uniform angular velocity between the cluster and small particles, hence:

$$\mathbf{u}_{p, CG} = \frac{1}{f_{CG}^3} \sum_{\forall p \in cell} \mathbf{u}_{p, orig} \quad (42)$$

and

$$\omega_{p, CG} = \frac{1}{f_{CG}^3} \sum_{\forall p \in cell} \omega_{p, orig}. \quad (43)$$

Accordingly, regarding particle-particle collisions the cluster of small particles is considered as colliding in an identical way with the requirement of the kinetic energy of the coarse grain particle lump being equal to the sum of the individual smaller particles:

$$\frac{1}{2} m_{p, CG} \mathbf{u}_{p, CG}^2 + \frac{1}{2} I_{p, CG} \omega_{p, CG}^2 = f_{CG}^3 \left( \frac{1}{2} m_p \mathbf{u}_p^2 + \frac{1}{2} I_p \omega_p^2 \right). \quad (44)$$

The contact forces, both in normal and tangential direction, for the cluster of coarse grained particles,  $\mathbf{F}_{n,CG}^c$  and  $\mathbf{F}_{t,CG}^c$ , respectively, are  $f_{CG}^3$ -times the contact forces of an original particle,  $\mathbf{F}_n^c$  and  $\mathbf{F}_t^c$ :

$$\mathbf{F}_{n,CG}^c = f_{CG}^3 \mathbf{F}_n^c \quad (45)$$

and

$$\mathbf{F}_{t,CG}^c = f_{CG}^3 \mathbf{F}_t^c. \quad (46)$$

The moment of inertia of the coarse grained cluster of particles  $I_{p,CG}$  can be calculated with the assumption of equal velocity between the coarse grained particle cluster and the individual particles (cf. Equation 42), as well as the following dependencies of the particle dimensions (cf. Equation 38) and masses of the coarse grained and small particles on the coarse grain factor  $f_{CG}$ :

$$m_{p,CG} = f_{CG}^3 m_{p,orig}. \quad (47)$$

Hence, the following relation for the moment of inertia is valid:

$$I_{p,CG} = f_{CG}^5 I_{p,orig}. \quad (48)$$

Furthermore, the torque of the coarse grained particle cluster  $\mathbf{T}_{p,CG}$  can be expressed with:

$$\mathbf{T}_{p,CG} = f_{CG}^4 \mathbf{T}_{p,orig}. \quad (49)$$

Typically, CFD-DEM simulations are applied for lab- to small scale applications and not for industrially relevant reactor sizes due to the high amount of particles. The simulation of industrially relevant scales was formerly limited to the TFM approach, but using a Lagrangian frame provides more detailed results than the Euler-Euler method [47, 48]. The number of particles with the CG method can be lowered and therefore the simulation time drastically reduced using CFD-DEM. Hence, the Euler-Lagrange approach with the CG method can be extended to a wider range of particle numbers, i.e., geometry scales, while still including its advantages, e.g., simulating individual particle properties and cohesion effects. A limitation for the CG method is the limited scaling of the parcels as the flow structures might not be depicted sufficiently anymore. Radl and Sundaresan [49] proposed a filtering approach to encounter this limitation. Yet another disadvantage when using the CG method is the resulting larger particle sizes, as the particle diameter limits the choice of the numerical grid size. For this special case the implementation of a multi-grid method can be useful to overcome this restriction.

## 2.2. Numerical solution

A parameter to quantify the stability of transient simulations was proposed by Courant et al. [50]:

$$Co = |\mathbf{u}_f| \frac{\Delta t}{\Delta x_{\text{cell}}}. \quad (50)$$

The Courant number  $Co$  describes how many cells a certain variable moves in a predefined time-step  $\Delta t$ . Depending on the velocity-pressure coupling algorithm the stability criterion is  $Co \leq 1$  [51] for the PISO-algorithm (Pressure-Implicit with Splitting of Operators) [52]. Table 1

summarizes the different discretization schemes used in the following simulations.

**Table 1:** Numerical discretization employed in the simulations.

Type	Scheme
Pressure-velocity coupling	PISO [52]
Time	first-order implicit
Gradient	non-limited Gauss linear
Momentum	QUICK

### 2.3. Multi-level grid method

A dual-grid method, i.e., using two separate numerical grids for CFD-DEM simulations was first proposed by Alobaid et al. [29]. Here, the flow of the fluid phase and the particles is calculated on separate numerical grids, distinguished by their resolution. Important parameters, e.g., the void fraction  $\varepsilon$  or the momentum exchange  $\mathbf{M}_{f,s}$ , are mapped between the different sized grids (cf. Figure 1), usually with a volume conservative mapping method [30]. The numerical grid for the fluid phase has usually more cells than the one used for the particles and therefore the resolution is higher.

The decrease in simulation speed due to more cells and interpolation errors due to the mapping procedure are the biggest disadvantages of the dual-grid method. The main advantage of a dual-grid method for CFD-DEM simulations is to overcome the restriction of minimum cell size due to the requirement of the cells being larger than the particles [30]. The traditional CFD-DEM, i.e., a single-grid method, can result in difficulties regarding this requirement, as either the cells

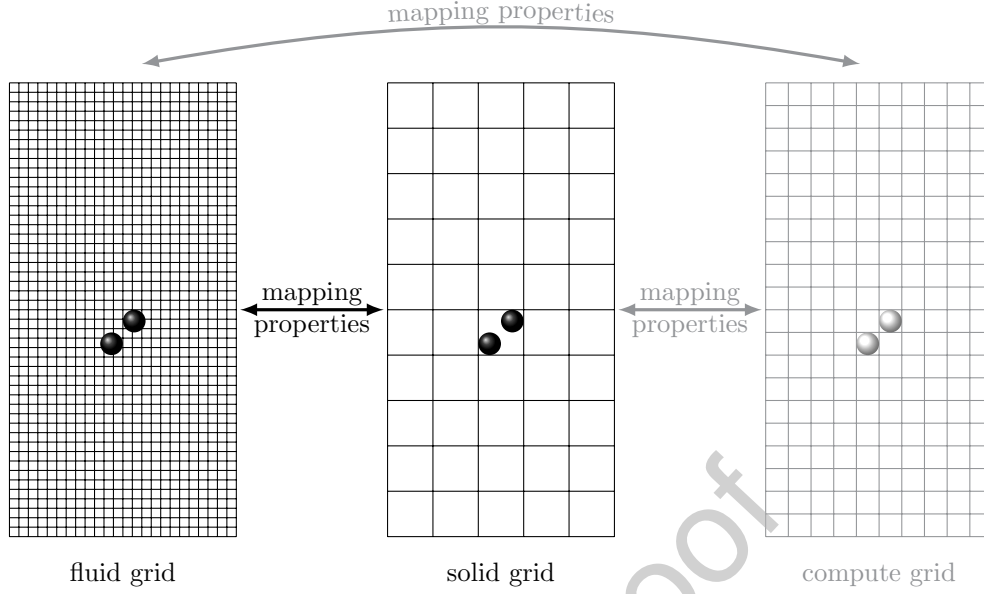


**Figure 1:** Overview of two and three (gray) different grid sizes for CFD-DEM multi-grid simulations with two exemplary particles indicated.

are larger than the particles which can result in a poor resolution of the fluid flow or the cell size is too small for the simulations to result in physically reasonable values or can have a negative impact on accuracy of the momentum exchange calculation between the fluid phase and particles. This issue is illustrated in Figure 2, as it depicts three uniform sized spherical particles in a cubic cell with a particle diameter to cell length of ( $d_p/l_{\text{cell}} = 0.75$ ). When using the commonly used and fast Particle Centroid Method (PCM) for void fraction determination [53, 54], a total of four different values for the void fraction  $\varepsilon$  can be obtained considering up to three particles are residing in the respected cell. In the case of particles overlapping the boundary of the cell and therefore the cell having enough void space to allocate another particle, the volume fraction of the fluid phase  $\varepsilon$  can result in a negative value and have a negative impact in numerical stability and an unphysical behavior. This is usually prevented by introducing a maximum packing limit serving

as a threshold, e.g., for randomly packed spheres  $\varepsilon_{\max} = 0.4$  [55]. When applying a maximum packing limit, the volume fraction of the fluid phase  $\varepsilon$  can have the following values:

- $\varepsilon = 1$  if no particles are present,
- $\varepsilon = 0.78$  if one particle is present,
- $\varepsilon = 0.56$  if two particles are present and
- $\varepsilon = \varepsilon_{\max}$  if three or more particles are present.

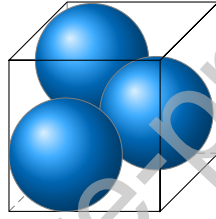
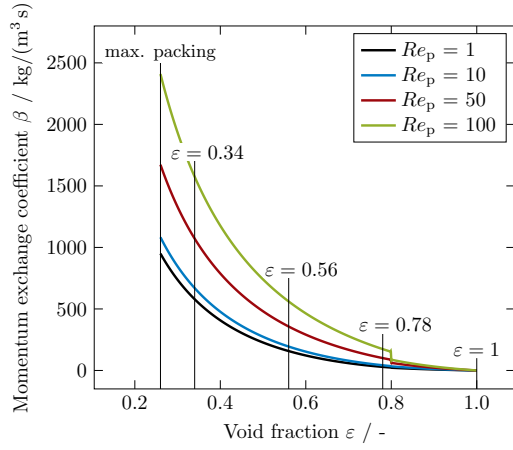


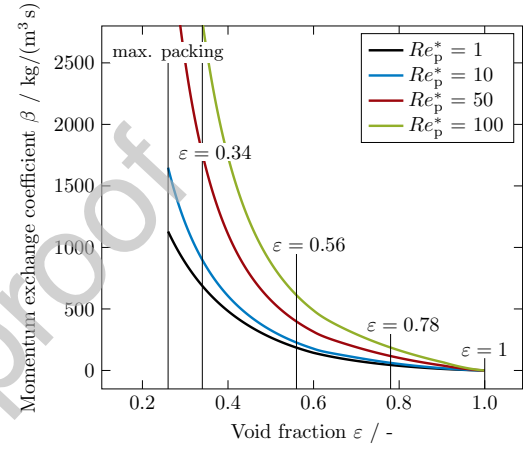
**Figure 2:** Simplified representation of a cubic cell with three uniform-sized particles

( $d_p/l_{\text{cell}} = 0.75$ ). The values of the fluid volume fraction  $\varepsilon$  with this  $d_p/l_{\text{cell}}$ -ratio are 1, 0.78, 0.56 and 0.34 for none, one, two and three particles using PCM.

The momentum exchange coefficient  $\beta$  in Equation 7 is highly dependent on the void fraction [56]. With the simplified assumption that the main contribution to the momentum exchange term is the drag force  $\mathbf{F}_D$ , it is obvious that the resolution of the momentum exchange calculated with conventional drag correlations, e.g., Gidaspow [37, 38], Hill-Koch-Ladd (HKL) [42, 43] or the extended HKL model [41], increases if the particle diameter to cell length ratio  $d_p/l_{\text{cell}}$  decreases, i.e., larger cells or smaller particles. Figure 3 depicts this relationship for the Gidaspow and extended HKL drag model for different particle Reynolds numbers, if four different values for the void fraction  $\varepsilon$  can be achieved due to three possible particles in a numerical cell.



(a) Gidaspow drag model.



(b) Extended HKL drag model with the modified particle Reynolds number

$$Re_p^* = 0.5Re_p.$$

**Figure 3:** Resulting momentum exchange coefficients  $\beta$  depending on the void fraction  $\varepsilon$  and particle Reynolds numbers. Indicated are the maximum packing limit and the four theoretical void fraction values if  $d_p/l_{\text{cell}} = 0.75$ , i.e., a total of maximum three particles can reside in the cell.

As can be seen, the gradient of the momentum exchange coefficient  $\beta$  becomes greater with lower void fraction  $\varepsilon$ , e.g., more particles. At these regions a greater resolution of the void fraction becomes more important for a correct momentum exchange calculation between the fluid phase and the particles. Fluidized bed reactors usually operate at a range of  $\varepsilon = 0.4$  to  $0.8$  [57, 58] and therefore this issue can be crucial for the simulation accuracy. Furthermore, the gradient of the momentum exchange coefficient increases with higher particle Reynolds numbers  $Re_p$ . High particle Reynolds numbers occur for example at high relative velocities between the fluid phase and particle  $|\mathbf{u}_f - \mathbf{u}_p|$  (cf. Equation 10). Those high relative velocities often occur in turbulent fluidized beds and in spouted fluidized beds. In conventional CFD-DEM simulations the volume fraction of the fluid phase  $\varepsilon$  is calculated on a single numerical grid and therefore the cell size is limited by the particle size. The particle size dependency can be overcome with the introduction of an additional numerical grid to decouple the fluid flow calculations and the Lagrangian particle tracking.

In this work, three different sizes for the numerical grids are used: a fluid, a solid and a compute grid. The fluid grid has the highest resolution, where the momentum balance and the continuity equation for the fluid phase are solved. The solid grid consists of the coarsest cells. This numerical grid is used to calculate the volume fractions of the solid phase  $\alpha$ . Important parameters to validate and evaluate the simulations are for example the volume fraction and the velocity of the solid phase,  $\alpha_s$  and  $\mathbf{u}_s$ . Using a dual-grid simulation, the quality of the resolution for those parameters would be poor, as the numerical grid is coarse. Therefore, another grid, the compute grid, is introduced. The resolution of this grid is finer compared to the solid grid, but still satisfies the condition of  $d_p/l_{\text{cell}} \leq 1$  to avoid unphysical values for the volume fraction.



The solving procedure for the three-level grid method is subdivided to the three different numerical grids according to Figure 4. The Lagrangian equations for the calculation of the particle velocities and movements are solved on the solid grid. The particles with the new positions and velocities are then mapped onto the compute grid. On this grid the Lagrangian properties are transformed to Eulerian field values. The resulting Eulerian fields, i.e., the volume fraction and the velocity of the solid phase,  $\alpha$  and  $\mathbf{u}_s$ , are then mapped to the fluid grid along with the force between the fluid phase and particles from the solid grid  $\mathbf{F}_{f,p}$ . The momentum exchange coefficient  $\beta$  between the fluid and solid phase used for the determination of  $\mathbf{F}_{f,p}$  is not calculated with the Eulerian field values from the finer compute grid, as the resolution for the solid phase fraction from the compute grid would be too low. Therefore, with the mapped solid phase fraction  $\alpha$  and the solid phase velocity  $\mathbf{u}_s$  from the compute grid, as well as the coupling forces between the fluid phase and particles  $\mathbf{F}_{f,p}$  from the solid grid, the momentum balance of the fluid phase can then be solved with those mapped parameters. The resulting new velocity and pressure field of the fluid phase is then mapped to the solid grid and the iteration loop starts again until the end time of the simulation is reached. The solving procedure for the dual-grid method is analogous, with the difference that the Eulerian field values for the solid phase fraction  $\alpha$  and the solid phase velocity  $\mathbf{u}_s$  are calculated on the solid grid instead of the compute grid.

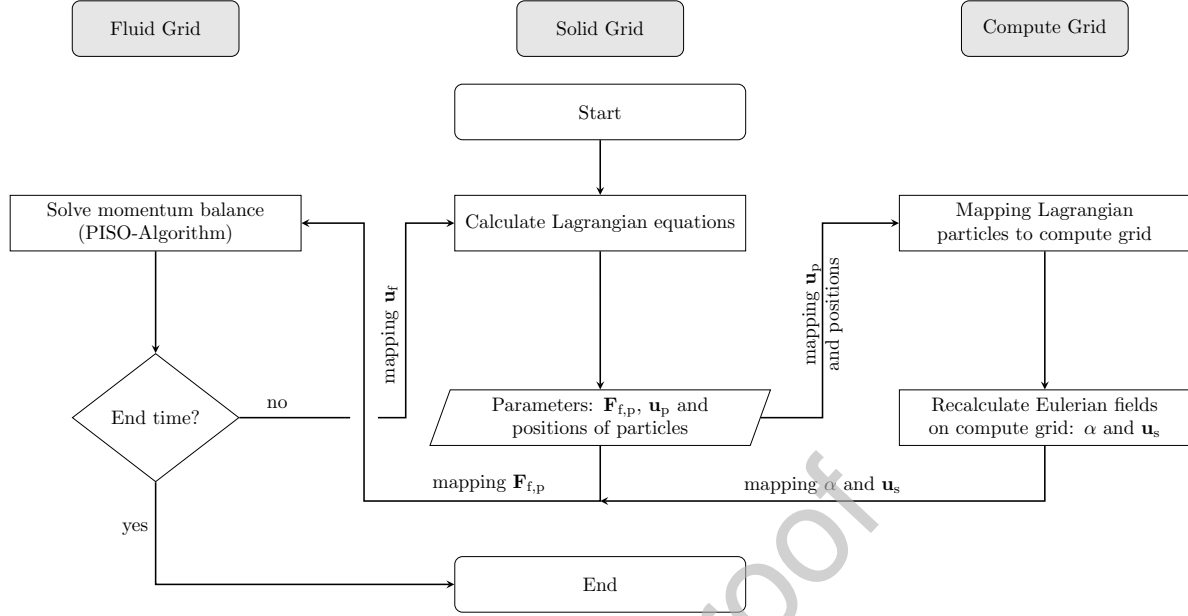


**Figure 4:** Solving procedure for the three-grid CFD-DEM simulation.

The simulations for the single-grid method were performed with the solver *DPMFoam* from the open-source package OpenFOAM® v4.x [59]. A detailed overview of the used solver *DPMFoam* can be found elsewhere [60]. The dual-grid method and the three-level grid approach were also implemented in OpenFOAM®.

### 3. Results and Discussion

The extended HKL model [41] was used in the following simulations to calculate the drag coefficient  $C_d$  as it was found to be most accurate in preliminary studies. In the following, the newly developed solver is validated and evaluated with three different experimental gas-solid fluidized beds:

- a jet-in fluidized bed by van Buijtenen et al. [61],

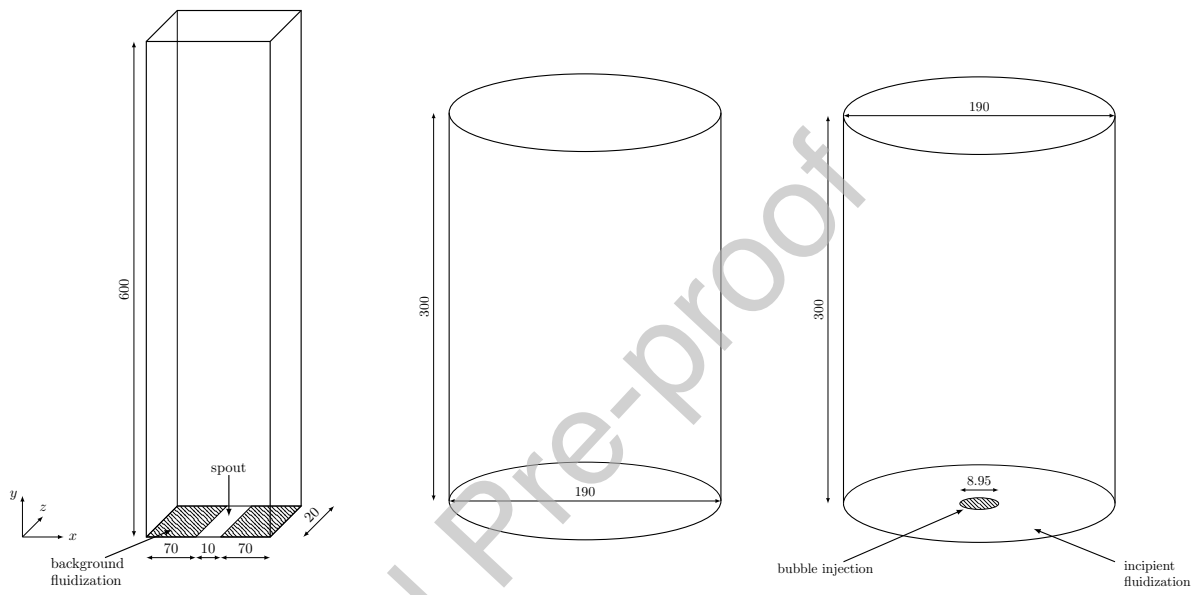
- a fluidized bed by Penn et al. [62] and
- an incipient fluidized bed with a single jet by Boyce et al. [63].

At last, the simulation time for each of the different approaches, i.e., single-grid, dual-grid and three-level grid approach will be presented and discussed.

### 3.1. Single-, dual- and three-level grid approach

For each of the three different validation cases, the commonly CFD-DEM approach with a single grid, a dual-grid and the newly developed three-level grid method is used for comparison in terms of simulation accuracy and speed. The smallest cell size of the different numerical grids used for Lagrangian calculations is chosen to be 1.6-times the particle diameter [28]. Although Peng et al. [28] proposed this critical cell size ratio specifically for CFD-DEM simulations using an analytical approach for the void fraction calculation, here, this threshold is used with the PCM, as we are investigating a multi-level grid approach. Regarding the dual- and three-level grid method, the cell-to-particle diameter ratios for the fluid, solid and compute grid are varied to get an optimal ratio for each grid.

In the following, the names of the simulations based on the different grid sizes used, are abbreviated according to the ratios of the numerical grid size to the recommendation by Peng et al. [28]. This means, the name for a simulation has three values for the fluid, compute and solid grid, i.e.,  $f_a-c_b-s_c$ , while  $f$ ,  $c$  and  $s$  stand for fluid, compute and solid grid and  $a$ ,  $b$  and  $c$  for a refinement ratio, if the value is lower than one, or for a coarsening, if the value is greater than one. For example, the single-grid approach is abbreviated with  $f_1-c_1-s_1$  and a dual-grid approach with the coarsening of the solid grid with a factor of 1.5 to its original size is represented by  $f_1-c_1-s_{1.5}$ . The index  $l$  is in



(a) Jet-in fluidized bed.

(b) Fluidized bed with CG.

(c) Single jet in an incipient fluidized bed with CG.

**Figure 5:** Simulation geometries for the pseudo 2D jet-in fluidized bed from van Buijtenen et al. [61] (a), the 3D cylindrical fluidized bed from Penn et al. [62] (b) and the 3D cylindrical incipient fluidized bed with a single jet from Boyce et al. [63] (c).

accordance to the recommendations of Peng et al. [28] using CFD-DEM simulations with PCM, i.e., the cell size is 3.82 times the particle diameter. The maximum refinement of the compute grid (index *max*) stands for the lower limit of the cell size, i.e., 1.63 times the particle diameter. Although, Peng et al. [28] explicitly stated the lower limit for the cell size is only suitable when using an analytical approach for the volume fraction determination, in our simulations, it is still used as the compute grid is not used to determine the crucial fluid-particle force  $\mathbf{F}_{f,p}$ .

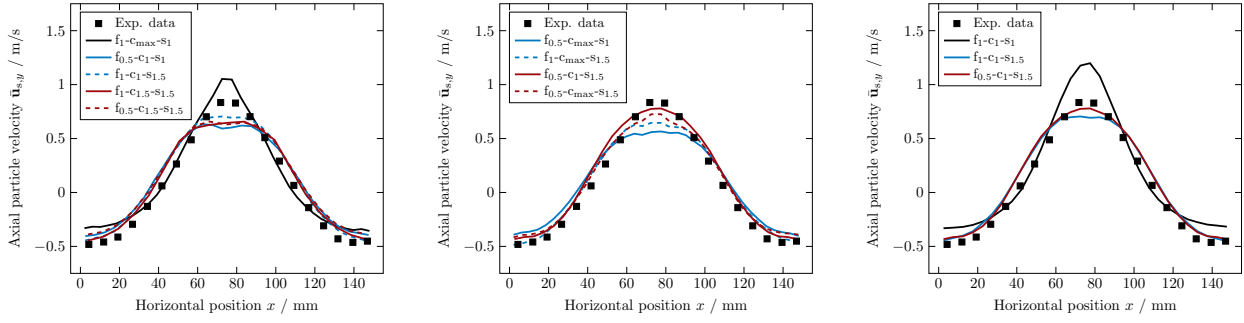
*Jet-in fluidized bed.* van Buijtenen et al. [61] measured the particle velocity of a pseudo 2D jet-in fluidized bed with positron emission particle tracking (PEPT) and particle image velocimetry (PIV). Figure 5a shows the pseudo 2D geometry used for the simulation. The height of the geometry in the simulation was reduced from 2500 mm used in the experiments to a total height of 600 mm. In preliminary studies it was found that the particle fountain never reached a height of 600 mm and therefore the total height of the geometry in the following simulations was reduced accordingly to decrease simulation time. Table 2 gives a brief overview of the simulation parameters used in the simulations. Further parameters and properties, e.g., normal or tangential coefficients of restitution,  $e_n$  and  $e_t$ , respectively, were chosen according to the publication of van Buijtenen et al. [61]. An overview of the number of cells in each direction and total number of cells for each individual simulation case, i.e., single-grid, dual-grid and three-level grid approaches, can be found in Table S1 in the Supplementary Material.

**Table 2:** Simulation parameters and properties used for the jet-in fluidized bed by van Buijtenen et al. [61].

Property	Value
Particle diameter $d_p$ / mm	3
Number of particles $n_p$	12 000, 14 000 and 17 000
Particle density $\rho_p$ / kg/m <sup>3</sup>	2505
Fluid phase	ambient conditions
Background velocity $\mathbf{u}_{bg}$ / m/s	4.15
Single jet velocity $\mathbf{u}_{jet}$ / m/s	37.25
Numerical grid for single-grid approach	
Number of cells in $x$ -direction $n_x$	30
Number of cells in $y$ -direction $n_y$	120
Number of cells in $z$ -direction $n_z$	2

The principle of ergodicity is used to obtain parameters in a dynamic system, i.e., a fluidized bed, which are comparable over time in a quasi steady-state. Therefore, the axial particle velocity of the particulate phase  $\mathbf{u}_{s,y}$  is time-averaged over a time-frame of 20 s to obtain the time-averaged axial velocity of the particulate phase  $\bar{\mathbf{u}}_{s,y}$ .

Figure 6 shows the experimental obtained time-averaged axial velocity of the solid phase  $\bar{\mathbf{u}}_{s,y}$  at an axial height of  $y = 100$  mm and the corresponding simulation results from the different single-, dual-grid and three-level grid approaches for a total of 12 000 initially settled particles.



(a) Comparison of dual-grid simulations. (b) Comparison of three-level grid simulations. (c) Single, dual-grid (best) and three-level grid approach (best).

**Figure 6:** Comparison of the experimental axial particle velocity  $\bar{u}_{s,y}$  at a lateral height of  $y = 100$  mm with simulation results of different refinements of grid sizes using a dual-grid approach (a), three-level grid approach (b) and a single-grid ( $f_1$ - $c_1$ - $s_1$ ) including the best results of the dual- and three-level grid for a total of 12 000 particles.

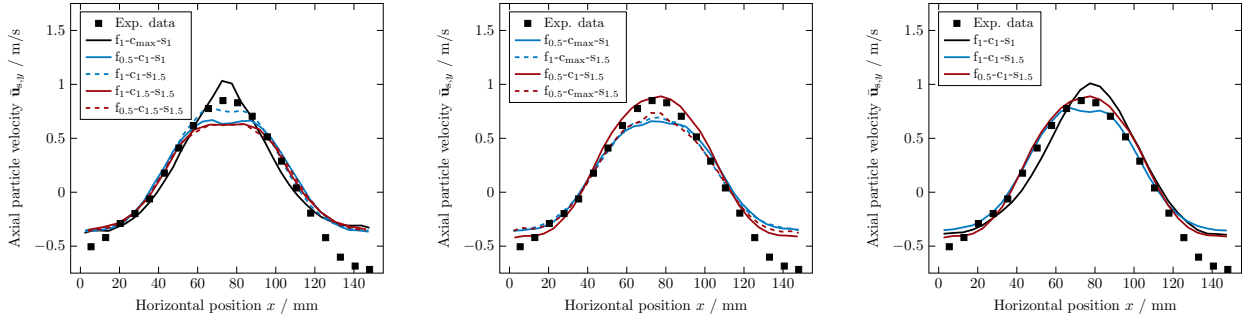
The resulting differences when varying the refinement and coarsening levels of the dual-grid approach are presented in Figure 6a. A solely refinement of the compute grid while not modifying the fluid and compute grid ( $f_1$ - $c_{\max}$ - $s_1$ ) shows an improvement of the resulting maximum axial particle velocity compared to the single grid approach. With the refinement of the compute grid the accuracy of the volume fraction of the solid phase and the resolution of the particle velocity is increased, thus leading to a higher overall accuracy. It can be also noted, that a refinement of the fluid grid and the coarsening of the solid grid lead to an improvement of the depiction for the solid phase flow behavior in the near-wall region. However, a coarsening of the solid grid is more beneficial towards an increase in accuracy than the refinement of the fluid grid. Concluding, the simulation results with the introduction of a dual-grid approach show a better agreement than the single-grid approach.

Figure 6b shows the effect of modifications to the different numerical grids for the three-level grid approach. The best agreement towards the experimental data is achieved when using a refinement of the fluid grid and a coarsening of the solid grid, i.e.,  $f_{0.5}-c_1-s_{1.5}$ , although all simulations with the three-level grid approach show a very good agreement in terms of accuracy.

Figure 6c compares the single-grid approach ( $f_1-c_1-s_1$ ) and the results from the dual-grid and three-level grid approach with the best cell-size refinement and coarsening configuration,  $f_1-c_1-s_{1.5}$  and  $f_{0.5}-c_1-s_{1.5}$ , respectively. In the core region of the geometry, where the jet-stream inlet is located, the highest particle velocities are observable in both experimental data and simulation results. Here, the simulation with the single-grid approach overpredicts the resulting axial particle velocity. The dual-grid and three-level approach show a better agreement for the maximum axial particle velocity than the single-grid approach in regards to the experimental data. The results from the three-level grid approach depict the experimental values best compared to the other approaches. Furthermore, in the near-wall region the results from the dual-grid and three-level grid approach are almost identical to the experimental data, while the single-grid approach has a higher agreement to the experimental values between the core area and the wall region. The overprediction of the axial velocity in the annulus region can be explained by the higher wall-effect in the pseudo 2D simulation compared to the 3D experiment. Still, the use of a multi-level grid approach shows a significant improvement in respect to the prediction of the particulate flow behavior than the simulation performed on a single grid.

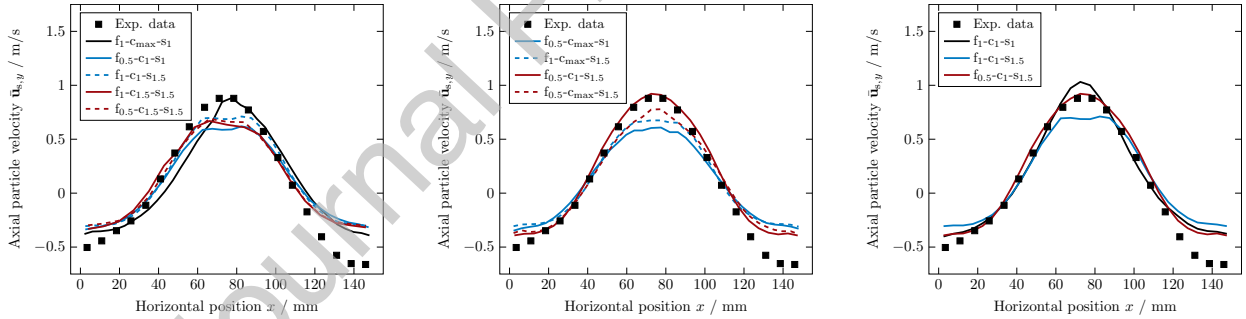
The results for the various multi-grid approaches with different refinement and coarsening levels, as well as the single-grid method compared to the experimental findings from van Buijtenen et al. [61] for a total of 14 000 and 17 000 initial particles are depicted in Figure 7 and Figure 8.





(a) Comparison of dual-grid simulations. (b) Comparison of three-level grid simulations. (c) Single, dual-grid (best) and three-level grid approach (best).

**Figure 7:** Comparison of the experimental axial particle velocity  $\bar{u}_{s,y}$  at a lateral height of  $y = 100$  mm with simulation results of different refinements of grid sizes using a dual-grid approach (a), three-level grid approach (b) and a single-grid ( $f_1$ - $c_1$ - $s_1$ ) including the best results of the dual- and three-level grid for a total of 14 000 particles.



(a) Comparison of dual-grid simulations. (b) Comparison of three-level grid simulations. (c) Single, dual-grid (best) and three-level grid approach (best).

**Figure 8:** Comparison of the experimental axial particle velocity  $\bar{u}_{s,y}$  at a lateral height of  $y = 100$  mm with simulation results of different refinements of grid sizes using a dual-grid approach (a), three-level grid approach (b) and a single-grid ( $f_1$ - $c_1$ - $s_1$ ) including the best results of the dual- and three-level grid for a total of 17 000 particles.

The same observations analogies to the simulation with 12 000 particles can be made for the simulations with 14 000 and 17 000 particles:

- the single-grid approach overpredicts the axial particle velocity in the core of the fluidized bed,
- a dual-grid method can depict the experimental values better than the single-grid method and
- the best agreement between the experimental data and the simulation results is achieved with the three-level grid approach.

The influence of the different refinement levels for the compute grid, i.e.,  $c_1$  and  $c_{\max}$ , where the volume fraction of the solid phase is calculated and mapped to the fluid grid and the velocity of the solid phase determined, is depicted in Figure 9 for a total of 12 000, 14 000 and 17 000 particles.

The best agreement between the experimental data and the simulation results can be achieved with the refinement levels of  $f_{0.5}-c_1-s_{1.5}$ . A refinement level of  $f_{0.5}-c_{\max}-s_{1.5}$ , i.e., a cell to particle diameter ratio of 1.6 for the compute grid cells, show a slightly worse accuracy. For most cases the maximum refinement of the compute grid ( $c_{\max}$ ) results in a decrease of the maximum axial particle velocity in the core area. Comparing the single-grid ( $f_1-c_1-s_1$ ) and the dual-grid approach with a maximum compute grid refinement ( $f_1-c_{\max}-s_1$ ), it is seen, that for all cases the refinement increases the accuracy and the experimental data is better depicted. However, an increase in cell-resolution for the compute grid does not always lead to a better accuracy in this particular case.

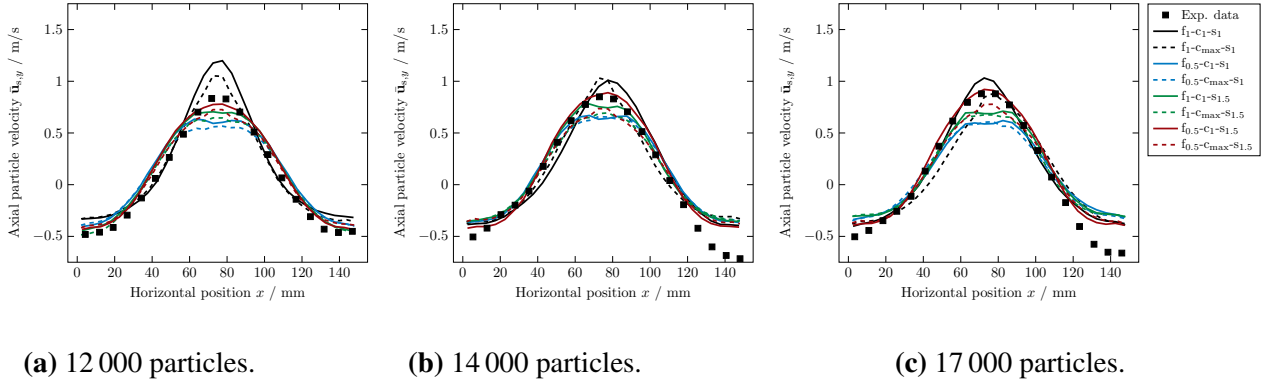


**Figure 9:** Comparison of the experimental axial particle velocity  $\bar{u}_{s,y}$  at a lateral height of  $y = 100$  mm with simulation results with different compute grid sizes for a total of 12 000, 14 000 and 17 000 particles.

*Fluidized bed with CG.* The fluidization behavior and bubble dynamics in a 3D cylindrical fluidized bed was investigated by Penn et al. [62] using magnetic resonance imaging (MRI). Two different sized particles of  $d_p = 1$  and 3 mm with three different initial bed heights of  $H_0 = 100$ , 150 and 200 mm were fluidized with up to five different inlet velocities having a velocity to minimum fluidization velocity ratio of  $\mathbf{u}_f/\mathbf{u}_{mf} = 1.2, 1.5, 2, 3$  and 4. The fluid used was air at ambient conditions. Here, for validation purposes, we are comparing the results of our simulations with the fluidized particles with a diameter of 1 mm. With the greatest settled bed height of 200 mm resulting in a total number of particles of close to seven million, it is obvious that a common CFD-DEM simulation would not be feasible. Therefore, the CG approach with a factor of four will be applied, i.e., 64 particles are considered as one parcel. Table 3 shows the simulation parameters used in the following. Due to the CG approach, the maximum number of tracked parcels can be reduced to approximately 100 000, which is in a reasonable range for a CFD-DEM simulation.

**Table 3:** Simulation parameters and properties used for the fluidized bed experiment of Penn et al. [62].

Property	Value
Particle diameter $d_{p, CG}$ / mm	4
CG factor	4
Number of particles $n_{p, CG}$	54 150, 81 225 and 108 300
Particle density $\rho_p$ / kg/m <sup>3</sup>	1040
Settled bed height $H_0$ / mm	100, 150 and 200
Fluid phase	ambient conditions
Inlet velocity ratios $\mathbf{u}_f / \mathbf{u}_{mf}$ / m/s	1.2, 1.5, 2, 3 and 4
Velocity at mf $\mathbf{u}_{mf}$ / m/s	0.25

Additional parameters and properties, e.g., the coefficient of restitution  $e$  or coefficient of friction  $\mu$  were adapted from Penn et al. [62]. Before presenting and discussing the simulation results of the different multi-grid approaches, it should be noted, that the overall geometry for the compute grid was slightly extended, if the compute and solid grid differed in cell size. At some refinement levels, the bounding domain of the two grids will not overlap (cf. Figure S1), resulting in a potential incorrect mapping of particles between the solid and compute grid. Further details and an analysis on the low impact towards the simulations results, when increasing the geometry of the compute grid, is given in Figure S2 in the Supplementary Material. The same geometry changes apply for the validation case based on the experiment of Boyce et al. [63] regarding the single jet

injection in an incipient fluidized bed.

A comparison of the simulation results using a single-grid approach ( $f_1$ - $c_1$ - $s_1$ ) with the experimental data for three different initial settled bed heights is depicted in Figure 10.

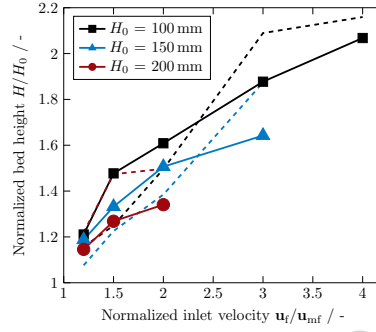


**Figure 10:** Simulation results of the normalized bed height  $H/H_0$  with different normalized inlet velocities  $u_f/u_{mf}$  for a single-grid approach (dashed lines) compared to the experimental data of Penn et al. [62] (marks and lines).

The simulations show an overall good agreement with the experimentally obtained normalized bed heights. The deviations between the normalized bed heights for an initial bed height of  $H_0 = 150$  mm at higher inlet velocities are in comparison with the experimental data higher than with the other initial settled bed heights of  $H_0 = 100$  and  $200$  mm. A qualitative comparison of the experimental data with the single-grid approach and various multi-grid approaches is depicted in Figure 11.

All single- and multi-level grid approaches slightly underpredict the resulting fluidized bed heights compared to the experimental finding obtained by Penn et al. [62] for lower inlet velocities, i.e.,  $u_f/u_{mf} \leq 2$ , and initial bed heights of  $100$  and  $150$  mm. At higher inlet velocities, the single- and dual-grid approach overpredict the normalized bed height in the fluidization state, while the

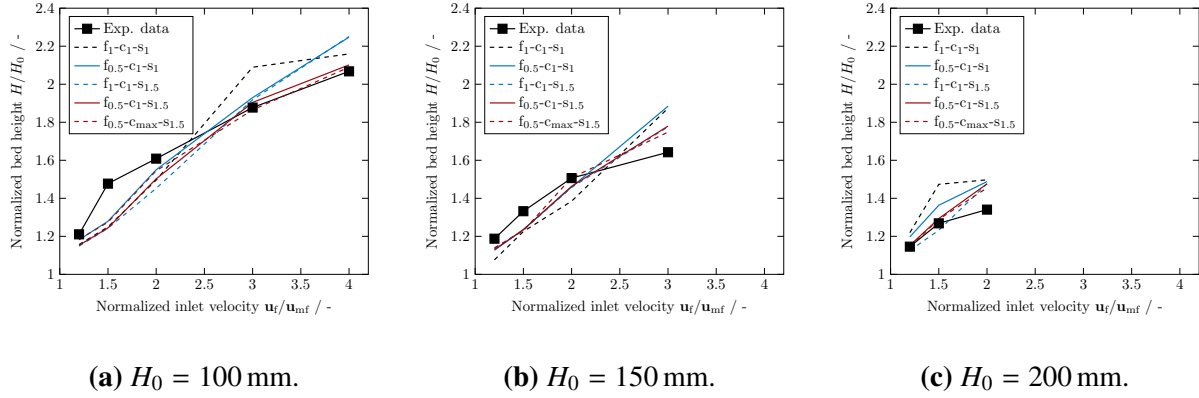


**Figure 11:** Comparison of experimental values of Penn et al. [62] with simulation results from the single-grid ( $f_1$ - $c_1$ - $s_1$ ), dual-grid and three-level grid approach with different refinement levels.

newly introduced three-level grid approach ( $f_{0.5}$ - $c_1$ - $s_{1.5}$  and  $f_{0.5}$ - $c_{\max}$ - $s_{1.5}$ ) shows a very good agreement with the experimental data. Furthermore, for an initial settled bed height of 200 mm the best results are obtained using the three-level grid approach. The use of a dual-grid approach results in a reasonable increase in accuracy for the fluidization behavior for all simulations, but with the introduction of a third numerical grid the best agreement towards the experimental data is achieved.

The deviations of the simulation results for various single-grid, dual-grid and three-level grid approaches from the experimental obtained normalized bed height  $H/H_0$  at different initial settled bed heights and inlet velocities are listed in Table 4.

**Table 4:** Deviation of simulation from experimental data regarding the ratio of expanded bed height to initial height  $H/H_0$  for the single-grid (S), dual-grid (D) and three-level grid approach (T).

			Type of grid	T	T	D	S	D
			$H/H_0$	Deviation simulation from exp. data				
$ \mathbf{u}_f/\mathbf{u}_{mf} $	Exp. data	f	0.5	0.5	0.5	1	1	
		c	max	1	1	1	1	
		s	1.5	1.5	1	1	1.5	
$H_0 = 100\text{ mm}$	1.2	1.21	2.1 %	2.1 %	2.4 %	4.5 %	2.3 %	
	1.5	1.48	13.9 %	13.9 %	15.5 %	15.6 %	13.8 %	
	2.0	1.61	4.2 %	4.0 %	3.8 %	6.8 %	4.7 %	
	3.0	1.88	1.2 %	1.1 %	2.5 %	10.6 %	1.9 %	
	4.0	2.07	0.7 %	2.0 %	3.1 %	4.1 %	2.6 %	
$H_0 = 150\text{ mm}$	1.2	1.19	4.1 %	4.8 %	5.1 %	9.4 %	4.4 %	
	1.5	1.33	7.7 %	7.3 %	7.2 %	8.0 %	7.4 %	
	2.0	1.51	0.1 %	2.9 %	3.1 %	8.1 %	3.3 %	
	3.0	1.64	6.4 %	8.4 %	14.7 %	14.1 %	8.1 %	
$H_0 = 200\text{ mm}$	1.2	1.15	0.1 %	0.5 %	4.5 %	6.4 %	1.8 %	
	1.5	1.27	1.7 %	2.0 %	7.5 %	16.2 %	2.9 %	
	2.0	1.34	8.5 %	10.1 %	11.0 %	11.7 %	10.1 %	

The use of a single-grid approach ( $f_1$ - $c_1$ - $s_1$ ) shows the worst agreement towards the experimental data compared to a dual-grid and three-level grid method. Refining the fluid grid or coarsening the solid grid increases the accuracy of the simulation results, but in most cases the coarsening of the solid grid has a more beneficial effect than the refinement of the fluid grid. The simultaneous refinement of the fluid grid and coarsening of the fluid grid with maintaining the compute grid as is, i.e.,  $f_{0.5}$ - $c_1$ - $s_{1.5}$  and  $f_{0.5}$ - $c_{\max}$ - $s_{1.5}$ , show a synergistic effect in improving further the accuracy and therefore lowering the deviation of the simulation results from the experimental data. All these observations are in accordance to the findings of the analysis of the jet-in fluidized bed benchmark case. Furthermore, the refinement of the compute grid up to the recommendations of Peng et al. [28] ( $f_{0.5}$ - $c_{\max}$ - $s_{1.5}$ ) has in almost all investigated cases a slightly better agreement in terms of accuracy towards the experimental data compared to the non refined compute grid ( $f_{0.5}$ - $c_1$ - $s_{1.5}$ ). However, the highest improvement of the accuracy can be contributed to the coarsening of the solid grid.

*Single jet injection in an incipient fluidized bed with CG.* The experimental set-up as used by Penn et al. [62] was used by Boyce et al. [63] and extended with a single jet injection hole. While the particles were fluidized, a single jet of air at ambient conditions was injected (cf. Figure 5c) and the bubble dimensions and dynamics were recorded. Table 5 gives an overview of the used simulation parameters. Analogous to the simulations validated with the experimental set-up by Penn et al. [62] a CG factor of  $f_{CG} = 4$  is used to reduce the computational costs. The number of cells for each of the following simulations is listed in Table S2.



**Table 5:** Simulation parameters and properties used for the single jet injection in an incipient fluidized bed by Boyce et al. [63].

Property	Value
Particle diameter $d_{p,CG}$ / mm	4
CG factor	4
Number of particles $n_{p,CG}$	108 300
Particle density $\rho_p$ / kg/m <sup>3</sup>	1040
Settled bed height $H_0$ / mm	200
Fluid phase	ambient conditions
Background velocity $\mathbf{u}_{bg}$ / m/s	0.25
Single jet velocity $\mathbf{u}_{jet}$ / m/s	52 and 85

Figures 12 and 13 show snapshots of the fountain in the fluidized of the experimental set-up and the simulations with different multi-grid approaches and refinements of each grid for jet velocities  $\mathbf{u}_{jet} = 52$  and  $85$  m/s.

In the experiments for both jet velocities, a narrow fountain is generated with bubbles forming and bursting when approaching the freeboard. An increase in the jet velocity results into an increase in bubble size in the fountain area. The simulations show qualitatively similar fountain shapes in the mid region. Furthermore, bubbles are also formed and begin to burst near the freeboard in accordance to the experimental observations by Boyce et al. [63]. The experimental size of the bubble just after the breakoff from the jet and deviation from the simulation results are

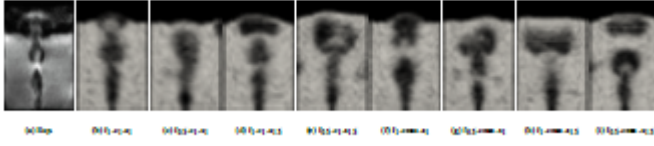


**Figure 12:** Instantaneous snapshots of single jet and bubble eruption in an incipiently fluidized bed with a jet velocity of  $u_{\text{jet}} = 52$  m/s for the experiment by Boyce et al. [63] (a). The simulations are performed various multi-grid approaches (b) to (i).

presented in Table 6.

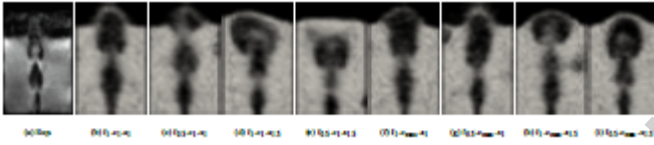


**Figure 13:** Instantaneous snapshots of single jet and bubble eruption in an incipiently fluidized bed with a jet velocity of  $u_{\text{jet}} = 85$  m/s for the experiment by Boyce et al. [63] (a). The simulations are performed various multi-grid approaches (b) to (i).

**Table 6:** Deviation of simulation from experimental data regarding the bubble volume  $V_{\text{bub}}$  for the single-grid (S), dual-grid (D) and three-level grid approach (T).

Type of grid		T	T	D	T	D	T	S	D
Exp. data		Deviation simulation from exp. data							
$ \mathbf{u}_{\text{jet}}  / \text{m/s}$	$V_{\text{bub}} / 10^{-5} \text{ m}^3$	f	0.5	0.5	0.5	0.5	1	1	1
		c	1	max	1	max	1	max	1
		s	1.5	1.5	1	1	1.5	1.5	1
52	2.56	3.4 %	4.1 %	19.6 %	13.3 %	8.6 %	10.6 %	37.5 %	28.9 %
85	3.79	0.3 %	1.4 %	32.9 %	11.2 %	6.1 %	4.9 %	25.3 %	24.3 %

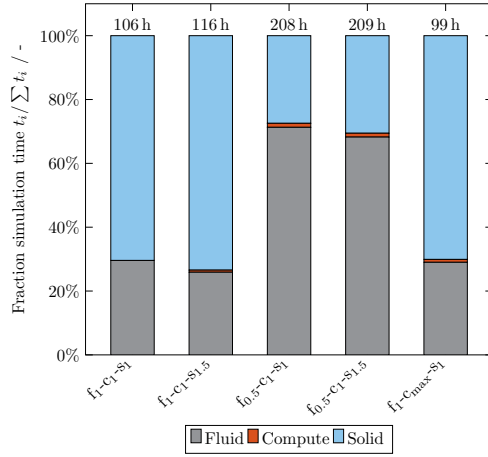
At first, it is seen that the coarse grain approach shows a good agreement between the experimental and simulation results. The used CG factor of  $f_{\text{CG}} = 4$  can be used for this specific setup to increase the simulation speed whilst still maintaining a reasonable accuracy. In accordance to the visual observations, the bubble size in the experiments increased with higher jet velocities  $\mathbf{u}_{\text{jet}}$ . The single grid approach ( $f_1$ - $c_1$ - $s_1$ ) shows the highest deviation from the experimental results of 28.9 % and 24.3 % for jet-velocities of 52 and 85 m/s, respectively. A refinement of the compute-grid ( $f_1$ - $c_{\text{max}}$ - $s_1$ ) results in a slight decrease in the deviation towards the experimental bubble size. Better results can be achieved with refining the fluid grid and coarsening the solid grid, i.e.,  $f_{0.5}$  and  $s_{1.5}$ . The best agreement between experiment and simulation is obtained with a simultaneously refinement and coarsening of the fluid and the solid grid, respectively, resulting in a deviation of less than 5 %. A change of the cell size of the compute grid for those particular cases has a negligible

effect on the accuracy. A comparison of the deviations for the multi-grid approach while varying the grid sizes of the compute grid, i.e.,  $f_x$ - $c_1$ - $s_y$  and  $f_x$ - $c_{\max}$ - $s_y$ , shows an overall improvement of the simulation results when applying a finer compute grid ( $c_{\max}$ ) with the exception of the multi-grid approaches of  $f_{0.5}$ - $s_{1.5}$  and  $f_1$ - $s_{1.5}$  at a jet velocity of  $\mathbf{u}_{\text{jet}} = 52 \text{ m/s}$ . A comparison between the multi-grid approaches, if either the fluid grid is refined ( $f_{0.5}$ ) or the solid grid is coarsened ( $s_{1.5}$ ) reveals that better results are obtained when using a coarsened solid grid instead of a finer fluid grid in accordance to the findings of Alobaid et al. [29]. This effect is mostly attributed to the better accuracy in determining and calculating the momentum exchange coefficient  $\beta$  for the fluid-solid coupling in the momentum balance.

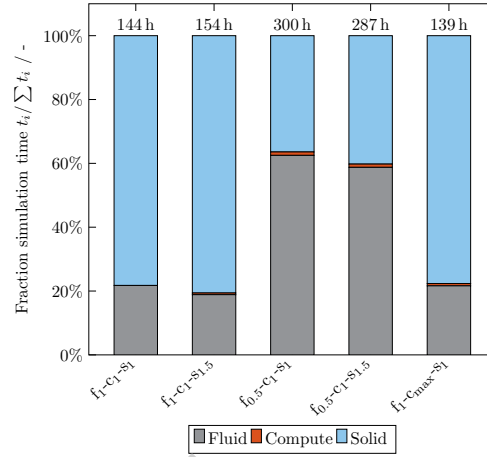
### 3.2. Simulation speed

Using an additional grid for numerical simulations always involves an increase in simulation time and resources, as important parameters must be mapped from one mesh to another. To quantify the additional simulation time needed with the implementation of a dual-grid and three-level grid method, several cases are set-up and investigated in terms of execution time used by the mapping process (compute grid), the calculation of the Lagrangian equations (solid grid) and the Eulerian equations (fluid grid). Figure 14 shows the simulation times needed for the jet-in fluidized bed case by van Buijtenen et al. [61] using five different grid-approaches, i.e., single-, dual-grid and three-level grid approach, for a total number of 12 000 and 17 000 particles.

It is obvious, that the simulation time increases with a higher number of particles due to the greater workload of the Lagrangian calculations. The execution time for the mapping procedures (*compute*) is zero for the single-grid  $f_1$ - $c_1$ - $s_1$  and for the dual-grid and three-level grid approaches



(a) 12 000 particles



(b) 17 000 particles

**Figure 14:** Resulting fractions of simulation times for the fluid, compute and solid grid to the total simulation time  $t_i / \sum t_i$  based on the jet-in fluidized bed with 12 000 and 17 000 particles with different single-, dual-grid and three-level grid approaches.

the time needed is negligible compared to the Eulerian (*fluid*) and Lagrangian (*solid*) calculations. The amount of the mapping time depends on the number of particles in the system and the cells of the fluid grid. Therefore, with an increase in total particles and a refinement of the fluid grid (cf.  $f_{0.5}-c_1-s_1$  for 17 000 particles) the time needed to transfer properties is greatest, but still marginal compared to the simulation times for the Eulerian and Lagrangian calculations. The fractions of the time needed to map all necessary properties to the total simulation time is between 0.5 and 1.7 %. The refinement of the fluid grid from 1 to 0.5 results in a massive increase of the simulation time due to the increased workload of the Eulerian calculations caused by the higher number of cells of said fluid grid. In these simulations the time-step was set to a constant value, as in this specific cases the  $Co$  number did not exceed the numerical stability criterion being a value of one. But a greater refinement of the numerical grid for the calculation of the fluid phase can

result in an additional large decrease in simulation speed due to not only the increasing number of computational cells, but a potentially needed decreased time-step. The smaller time-step originates from the dependency of the  $Co$  number from the cell size. In order to assure a constant  $Co$  number with smaller cells, the time step has to decrease as well (cf. Equation 50) and the simulation speed therefore slows down. Especially for multiphase flows with high velocities the time-step needs to be adjusted to assure the numerical stability of  $Co \leq 1$ .

#### 4. Conclusion

A conventional CFD-DEM simulation for gas-solid flow using a single-grid for the Eulerian and the Lagrangian equations was compared to a dual-grid method and a newly proposed three-level approach with the introduction of another numerical grid. Different experimental gas-solid flows, a 2D jet-in fluidized bed, a 3D cylindrical fluidized bed and a 3D cylindrical fluidized bed with a single jet, were used to validate the simulation results. Several conclusions can be made:

- the use of a multi-grid approach compared to a single-grid method results in an increase in accuracy,
- in most cases the three-level grid approach depicts the experimental data better than the dual-grid approach,
- when using a multi-grid approach, a coarsening of the Lagrangian grid results in a greater improvement in accuracy than the refinement of the Eulerian grid,
- the increase in simulation time due to the additional mapping subroutines in a multi-grid approach is negligible,

- with the use of the coarse grain method, the simulation time can be drastically reduced while still maintaining a suitable cell size for CFD-DEM simulations and
- the limiting factor of the multi-grid approach regarding simulation time is the degree of refinement of the Eulerian grid.

The set-up of a CFD-DEM simulation using a multi-grid approach requires a longer time, especially for the determination of suitable numerical grids, as two or three numerical grids have to be chosen. The necessary time needed to map the properties between the different grids is dependent on the number of particles and the number of cells of the fluid grid. An inadequate choice of the Eulerian grid can result in an enormous increase in simulation time with only a slight improvement of the accuracy. Still, the use of a multi-grid approaches is a promising tool to further increase the accuracy for dense solid flow simulations when larger particles are present. The use of more sophisticated methods for the transformation of Lagrangian values to Eulerian field values, e.g., porous cube model or diffusion-based model, with the use of the multi-level grid approach can be further investigated in terms of improvement in accuracy and change in simulation speed.

Further applications, e.g., the consideration of temperature changes or other parameters, can be made and if needed, calculated on different numerical grids. Therefore, the multi-grid approach is not limited to a two- or a three-level grid approach. The extension of this approach to polydisperse or cohesive particles is also possible. The simulation of bidisperse particles has already been done by Farzaneh et al. [33]. Hence, the polydispersity with a wide range of particle diameters shall be possible with the introduction of several grids for predefined particle diameter ranges.

## **Acknowledgments**

D. Hirche is thankful for the support from TUM Graduate School.

Journal Pre-proof



## Nomenclature

### *Alphabets*

$b$	parameter for spring theory, -
$C$	coefficient, -
$Co$	Courant number, -
$d$	diameter, m
$E$	Young's modulus, $\text{kg}/(\text{m s}^2)$
$e$	coefficient of restitution, -
$F$	dimensionless drag force, -
$\mathbf{F}$	force, $\text{kg m/s}^2$
$f_{CG}$	coarse grain factor, -
$\mathbf{g}$	gravitational acceleration, $\text{m/s}^2$
$H$	height, m
$\bar{\mathbf{I}}$	unit tensor, -
$I$	moment of inertia, $\text{kg m}^2$
$k$	spring stiffness, $\text{kg/s}^2$
$l$	length, m
$\mathbf{M}$	momentum, $\text{kg}/(\text{m}^2 \text{s}^2)$
$M_{\text{red}}$	reduced mass, kg
$m$	mass, kg
$n$	number, -

$\mathbf{n}$	unit vector in normal direction, -
$p$	pressure, kg/(m s <sup>2</sup> )
$Re$	Reynolds number, -
$r$	radius, m
$t$	time, s
$\mathbf{t}$	unit vector in tangential direction, -
$\mathbf{T}$	torque, kg m <sup>2</sup> /s <sup>2</sup>
$\mathbf{u}$	velocity, m/s
$V$	volume, m <sup>3</sup>
$w$	parameter for HKL-drag correlation, -

### *Greek Symbols*

$\alpha$	volume fraction solid phase, -
$\alpha_n$	related to coefficient of restitution, -
$\beta$	momentum exchange coefficient, kg/(m <sup>3</sup> s)
$\varepsilon$	volume fraction fluid phase, -
$\eta$	damping coefficient, -
$\mu$	viscosity, kg/(m s)
$\mu_f$	friction coefficient, kg/(m s)
$\nu$	Poisson Ratio, -

$\omega$	angular velocity, 1/s
$\rho$	density, kg/m <sup>3</sup>
$\overline{\tau}$	viscous stress tensor, kg/(m s <sup>2</sup> )

### *Subscripts*

b	buoyancy
bg	background
bub	bubble
CG	coarse grain
d	drag
e	effective
f	fluid phase
g	gravity
max	maximum
mf	minimum fluidization
n	normal
ol	overlap
orig	original
p	particle
rel	relative

s        solid phase  
t        tangential

### *Superscripts*

c                contact  
nc               non-contact

### **References**

- [1] W. Zhong, A. Yu, G. Zhou, J. Xie, H. Zhang, CFD simulation of dense particulate reaction system: Approaches, recent advances and applications, *Chemical Engineering Science* 140 (2016) 16–43, doi:\let\@tempa\bibinfo@X@doi10.1016/j.ces.2015.09.035.
- [2] J. Li, D. J. Mason, A. S. Mujumdar, A Numerical Study of Heat Transfer Mechanisms in Gas–Solids Flows Through Pipes Using a Coupled CFD and DEM Model, *Drying Technology* 21 (9) (2003) 1839–1866, doi:\let\@tempa\bibinfo@X@doi10.1081/drt-120025511.
- [3] F. P. D. Maio, A. D. Renzo, D. Trevisan, Comparison of heat transfer models in DEM-CFD simulations of fluidized beds with an immersed probe, *Powder Technology* 193 (3) (2009) 257–265, doi:\let\@tempa\bibinfo@X@doi10.1016/j.powtec.2009.03.002.
- [4] Y.-Q. Zhuang, X.-M. Chen, Z.-H. Luo, J. Xiao, CFD–DEM modeling of gas–solid flow and catalytic MTO reaction in a fluidized bed reactor, *Computers & Chemical Engineering* 60 (2014) 1–16, doi:\let\@tempa\bibinfo@X@doi10.1016/j.compchemeng.2013.08.007.
- [5] X. Ku, T. Li, T. Løvås, CFD–DEM simulation of biomass gasification with steam in a fluidized bed reactor,

- Chemical Engineering Science 122 (2015) 270–283, doi:\let\@tempa\bibinfo@X@doi10.1016/j.ces.2014.08.045.
- [6] P. Ostermeier, F. Fischer, S. Fendt, S. DeYoung, H. Spliethoff, Coarse-grained CFD-DEM simulation of biomass gasification in a fluidized bed reactor, *Fuel* 255 (2019) 115790, doi:\let\@tempa\bibinfo@X@doi10.1016/j.fuel.2019.115790.
- [7] S. Golshan, R. Sotudeh-Gharebagh, R. Zarghami, N. Mostoufi, B. Blais, J. Kuipers, Review and implementation of CFD-DEM applied to chemical process systems, *Chemical Engineering Science* 221 (2020) 115646, doi:\let\@tempa\bibinfo@X@doi10.1016/j.ces.2020.115646.
- [8] P. A. Cundall, O. D. L. Strack, A discrete numerical model for granular assemblies, *Géotechnique* 29 (1) (1979) 47–65, doi:\let\@tempa\bibinfo@X@doi10.1680/geot.1979.29.1.47.
- [9] Y. Tsuji, T. Tanaka, T. Ishida, Lagrangian numerical simulation of plug flow of cohesionless particles in a horizontal pipe, *Powder Technol.* 71 (3) (1992) 239–250, doi:\let\@tempa\bibinfo@X@doi10.1016/0032-5910(92)88030-1.
- [10] Y. Tsuji, T. Kawaguchi, T. Tanaka, Discrete particle simulation of two-dimensional fluidized bed, *Powder Technol.* 77 (1) (1993) 79–87, doi:\let\@tempa\bibinfo@X@doi10.1016/0032-5910(93)85010-7.
- [11] H. Enwald, E. Peirano, A.-E. Almstedt, Eulerian two-phase flow theory applied to fluidization, *Int. J. Multiphase Flow* 22 (1996) 21–66, doi:\let\@tempa\bibinfo@X@doi10.1016/s0301-9322(96)90004-x.
- [12] R. Jackson, Locally averaged equations of motion for a mixture of identical spherical particles and a Newtonian fluid, *Chemical Engineering Science* 52 (15) (1997) 2457–2469, doi:\let\@tempa\bibinfo@X@doi10.1016/s0009-2509(97)00065-1.
- [13] N. G. Deen, E. Peters, J. T. Padding, J. Kuipers, Review of direct numerical simulation of fluid–particle mass, momentum and heat transfer in dense gas–solid flows, *Chemical Engineering Science* 116 (2014) 710–724, doi:\let\@tempa\bibinfo@X@doi10.1016/j.ces.2014.05.039.
- [14] J. Link, L. Cuypers, N. Deen, J. Kuipers, Flow regimes in a spout–fluid bed: A combined experimental and simulation study, *Chemical Engineering Science* 60 (13) (2005) 3425–3442, doi:\let\@tempa\bibinfo@X@doi10.1016/j.ces.2005.01.027.

- [15] A. D. Renzo, F. P. D. Maio, Homogeneous and bubbling fluidization regimes in DEM–CFD simulations: Hydrodynamic stability of gas and liquid fluidized beds, *Chemical Engineering Science* 62 (1-2) (2007) 116–130, doi:\let\@tempa\bibinfo@X@doi10.1016/j.ces.2006.08.009.
- [16] S. Yang, Y. Sun, L. Zhang, Y. Zhao, J. W. Chew, Numerical investigation on the effect of draft plates on spouting stability and gas–solid characteristics in a spout-fluid bed, *Chemical Engineering Science* 148 (2016) 108–125, doi:\let\@tempa\bibinfo@X@doi10.1016/j.ces.2016.03.010.
- [17] D. Geldart, Types of gas fluidization, *Powder Technology* 7 (5) (1973) 285–292, doi:\let\@tempa\bibinfo@X@doi10.1016/0032-5910(73)80037-3.
- [18] M. Detamore, M. Swanson, K. Frender, C. Hrenya, A kinetic-theory analysis of the scale-up of circulating fluidized beds, *Powder Technology* 116 (2-3) (2001) 190–203, doi:\let\@tempa\bibinfo@X@doi10.1016/s0032-5910(00)00397-1.
- [19] V. Verma, N. G. Deen, J. T. Padding, J. Kuipers, Two-fluid modeling of three-dimensional cylindrical gas–solid fluidized beds using the kinetic theory of granular flow, *Chemical Engineering Science* 102 (2013) 227–245, doi:\let\@tempa\bibinfo@X@doi10.1016/j.ces.2013.08.002.
- [20] C. Moliner, F. Marchelli, N. Spanachi, A. Martinez-Felipe, B. Bosio, E. Arato, CFD simulation of a spouted bed: Comparison between the Discrete Element Method (DEM) and the Two Fluid Model (TFM), *Chemical Engineering Journal* 377 (2019) 120466, doi:\let\@tempa\bibinfo@X@doi10.1016/j.cej.2018.11.164.
- [21] M. Sakai, S. Koshizuka, Large-scale discrete element modeling in pneumatic conveying, *Chemical Engineering Science* 64 (3) (2009) 533–539, doi:\let\@tempa\bibinfo@X@doi10.1016/j.ces.2008.10.003.
- [22] M. Sakai, M. Abe, Y. Shigeto, S. Mizutani, H. Takahashi, A. Viré, J. R. Percival, J. Xiang, C. C. Pain, Verification and validation of a coarse grain model of the DEM in a bubbling fluidized bed, *Chemical Engineering Journal* 244 (2014) 33–43, doi:\let\@tempa\bibinfo@X@doi10.1016/j.cej.2014.01.029.
- [23] K. Chu, J. Chen, A. Yu, Applicability of a coarse-grained CFD–DEM model on dense medium cyclone, *Minerals Engineering* 90 (2016) 43–54, doi:\let\@tempa\bibinfo@X@doi10.1016/j.mineng.2016.01.020.
- [24] K. Takabatake, Y. Mori, J. G. Khinast, M. Sakai, Numerical investigation of a coarse-grain discrete element method in solid mixing in a spouted bed, *Chemical Engineering Journal* 346 (2018) 416–426, doi:\let\@tempa\bibinfo@X@doi10.1016/j.cej.2018.03.010.

bibinfo@X@doi10.1016/j.ccej.2018.04.015.

- [25] J. E. Hilton, P. W. Cleary, Comparison of non-cohesive resolved and coarse grain DEM models for gas flow through particle beds, *Applied Mathematical Modelling* 38 (17-18) (2014) 4197–4214, doi:\let\@tempa\bibinfo@X@doi10.1016/j.apm.2014.02.013.
- [26] A. Stroh, F. Alobaid, M. von Bohnstein, J. Strhle, B. Eppe, Numerical CFD simulation of 1 MWth circulating fluidized bed using the coarse grain discrete element method with homogenous drag models and particle size distribution, *Fuel Processing Technology* 169 (2018) 84–93, doi:\let\@tempa\bibinfo@X@doi10.1016/j.fuproc.2017.09.014.
- [27] A. Stroh, A. Daikeler, M. Nikku, J. May, F. Alobaid, M. von Bohnstein, J. Strhle, B. Eppe, Coarse grain 3D CFD-DEM simulation and validation with capacitance probe measurements in a circulating fluidized bed, *Chemical Engineering Science* 196 (2019) 37–53, doi:\let\@tempa\bibinfo@X@doi10.1016/j.ces.2018.11.052.
- [28] Z. Peng, E. Doroodchi, C. Luo, B. Moghtaderi, Influence of void fraction calculation on fidelity of CFD-DEM simulation of gas-solid bubbling fluidized beds, *AIChE Journal* 60 (6) (2014) 2000–2018, doi:\let\@tempa\bibinfo@X@doi10.1002/aic.14421.
- [29] F. Alobaid, J. Strhle, B. Eppe, Extended CFD/DEM model for the simulation of circulating fluidized bed, *Advanced Powder Technology* 24 (1) (2013) 403–415, doi:\let\@tempa\bibinfo@X@doi10.1016/j.appt.2012.09.003.
- [30] J. Su, Z. Gu, C. Chen, X. Y. Xu, A two-layer mesh method for discrete element simulation of gas-particle systems with arbitrarily polyhedral mesh, *International Journal for Numerical Methods in Engineering* 103 (10) (2015) 759–780, doi:\let\@tempa\bibinfo@X@doi10.1002/nme.4911.
- [31] F. Alobaid, A particle-grid method for Euler-Lagrange approach, *Powder Technology* 286 (2015) 342–360, doi:\let\@tempa\bibinfo@X@doi10.1016/j.powtec.2015.08.019.
- [32] S. Deb, D. K. Tafti, A novel two-grid formulation for fluid-particle systems using the discrete element method, *Powder Technology* 246 (2013) 601–616, doi:\let\@tempa\bibinfo@X@doi10.1016/j.powtec.2013.06.014.
- [33] M. Farzaneh, S. Sasic, A.-E. Almstedt, F. Johnsson, D. Pallarès, A novel multigrid technique for Lagrangian modeling of fuel mixing in fluidized beds, *Chemical Engineering Science* 66 (22) (2011) 5628–5637, doi:\let\

@tempa\bibinfo@X@doi10.1016/j.ces.2011.07.060.

- [34] R. Sun, H. Xiao, Diffusion-based coarse graining in hybrid continuum–discrete solvers: Applications in CFD–DEM, *International Journal of Multiphase Flow* 72 (2015) 233–247, doi:\let\@tempa\bibinfo@X@doi10.1016/j.ijmultiphaseflow.2015.02.014.
- [35] R. Sun, H. Xiao, Diffusion-based coarse graining in hybrid continuum–discrete solvers: Theoretical formulation and a priori tests, *International Journal of Multiphase Flow* 77 (2015) 142–157, doi:\let\@tempa\bibinfo@X@doi10.1016/j.ijmultiphaseflow.2015.08.014.
- [36] K. Papadakis, A. Bridgwater, S. Gu, CFD modelling of the fast pyrolysis of biomass in fluidised bed reactors, Part A: Eulerian computation of momentum transport in bubbling fluidised beds, *Chemical Engineering Science* 63 (16) (2008) 4218–4227, doi:\let\@tempa\bibinfo@X@doi10.1016/j.ces.2008.05.045.
- [37] J. Ding, D. Gidaspow, A bubbling fluidization model using kinetic theory of granular flow, *AIChE J.* 36 (4) (1990) 523–538, doi:\let\@tempa\bibinfo@X@doi10.1002/aic.690360404.
- [38] D. Gidaspow, *Multiphase Flow and Fluidization: Continuum and Kinetic Theory Descriptions*, Academic press, 1994.
- [39] S. Ergun, Fluid flow through packed columns, *Chem. Eng. Prog.* 48 (1952) 89–94.
- [40] C. Y. Wen, Y. H. Yu, Mechanics of fluidization, in: *Chem. Eng. Prog. Symp. Ser.*, vol. 62, 100–111, 1966.
- [41] S. Benyahia, M. Syamlal, T. J. O'Brien, Extension of Hill–Koch–Ladd drag correlation over all ranges of Reynolds number and solids volume fraction, *Powder Technol.* 162 (2) (2006) 166–174, doi:\let\@tempa\bibinfo@X@doi10.1016/j.powtec.2005.12.014.
- [42] R. J. Hill, D. Koch, A. J. C. Ladd, The first effects of fluid inertia on flows in ordered and random arrays of spheres, *Journal of Fluid Mechanics* 448 (2001) 213–241, doi:\let\@tempa\bibinfo@X@doi10.1017/s0022112001005948.
- [43] R. J. Hill, D. Koch, A. J. C. Ladd, Moderate-Reynolds-number flows in ordered and random arrays of spheres, *Journal of Fluid Mechanics* 448 (2001) 243–278, doi:\let\@tempa\bibinfo@X@doi10.1017/s0022112001005936.
- [44] A. D. Renzo, F. P. D. Maio, Comparison of contact-force models for the simulation of collisions in DEM-based



- granular flow codes, *Chemical Engineering Science* 59 (3) (2004) 525–541, doi:\let\@tempa\bibinfo@X@doi10.1016/j.ces.2003.09.037.
- [45] D. Zhang, W. Whiten, The calculation of contact forces between particles using spring and damping models, *Powder Technology* 88 (1) (1996) 59–64, doi:\let\@tempa\bibinfo@X@doi10.1016/0032-5910(96)03104-x.
- [46] N. Deen, M. V. S. Annaland, M. V. der Hoef, J. Kuipers, Review of discrete particle modeling of fluidized beds, *Chemical Engineering Science* 62 (1-2) (2007) 28–44, doi:\let\@tempa\bibinfo@X@doi10.1016/j.ces.2006.08.014.
- [47] B. van Wachem, S. Sasic, Derivation, simulation and validation of a cohesive particle flow CFD model, *AIChE Journal* 54 (1) (2007) 9–19, doi:\let\@tempa\bibinfo@X@doi10.1002/aic.11335.
- [48] V. Salikov, S. Antonyuk, S. Heinrich, V. S. Sutkar, N. G. Deen, J. Kuipers, Characterization and CFD-DEM modelling of a prismatic spouted bed, *Powder Technology* 270 (2015) 622–636, doi:\let\@tempa\bibinfo@X@doi10.1016/j.powtec.2014.05.026.
- [49] S. Radl, S. Sundaresan, A drag model for filtered Euler–Lagrange simulations of clustered gas–particle suspensions, *Chemical Engineering Science* 117 (2014) 416–425, doi:\let\@tempa\bibinfo@X@doi10.1016/j.ces.2014.07.011.
- [50] R. Courant, K. Friedrichs, H. Lewy, Über die partiellen Differenzengleichungen der mathematischen Physik, *Mathematische annalen* 100 (1) (1928) 32–74.
- [51] J. H. Ferziger, M. Perić, *Computational methods for fluid dynamics*, Springer, 2002.
- [52] R. Issa, Solution of the implicitly discretised fluid flow equations by operator-splitting, *Journal of Computational Physics* 62 (1) (1986) 40–65, doi:\let\@tempa\bibinfo@X@doi10.1016/0021-9991(86)90099-9.
- [53] Z. Peng, B. Moghtaderi, E. Doroodchi, A modified direct method for void fraction calculation in CFD–DEM simulations, *Advanced Powder Technology* 27 (1) (2016) 19–32, doi:\let\@tempa\bibinfo@X@doi10.1016/j.appt.2015.10.021.
- [54] L. Wang, J. Ouyang, C. Jiang, Direct calculation of voidage in the fine-grid CFD–DEM simulation of fluidized beds with large particles, *Particuology* 40 (2018) 23–33, doi:\let\@tempa\bibinfo@X@doi10.1016/j.partic.2017.11.010.

- [55] F. Marchelli, C. Moliner, B. Bosio, E. Arato, A CFD-DEM sensitivity analysis: The case of a pseudo-2D spouted bed, *Powder Technology* 353 (2019) 409–425, doi:\let\@tempa\bibinfo@X@doi10.1016/j.powtec.2019.05.035.
- [56] R. Stanly, G. Shoev, Detailed analysis of recent drag models using multiple cases of mono-disperse fluidized beds with Geldart-B and Geldart-D particles, *Chemical Engineering Science* 188 (2018) 132–149, doi:\let\@tempa\bibinfo@X@doi10.1016/j.ces.2018.05.030.
- [57] J. R. Grace, Contacting modes and behaviour classification of gas-solid and other two-phase suspensions, *The Canadian Journal of Chemical Engineering* 64 (3) (1986) 353–363, doi:\let\@tempa\bibinfo@X@doi10.1002/cjce.5450640301.
- [58] D. Kunii, O. Levenspiel, *Fluidization engineering*, Butterworth-Heinemann, Boston, 2 edn., ISBN 0409902330, 1991.
- [59] H. G. Weller, G. Tabor, H. Jasak, C. Fureby, A tensorial approach to computational continuum mechanics using object-oriented techniques, *Comput. Phys.* 12 (6) (1998) 620, doi:\let\@tempa\bibinfo@X@doi10.1063/1.168744.
- [60] C. Fernandes, D. Semyonov, L. L. Ferrás, J. M. Nóbrega, Validation of the CFD-DPM solver DPMFoam in OpenFOAM® through analytical, numerical and experimental comparisons, *Granular Matter* 20 (4), doi:\let\@tempa\bibinfo@X@doi10.1007/s10035-018-0834-x.
- [61] M. van Buijtenen, K. Buist, N. Deen, J. Kuipers, T. Leadbeater, D. Parker, Numerical and experimental study on spout elevation in spout-fluidized beds, *AIChE Journal* 58 (8) (2011) 2524–2535, doi:\let\@tempa\bibinfo@X@doi10.1002/aic.12765.
- [62] A. Penn, C. M. Boyce, T. Kovar, T. Tsuji, K. P. Pruessmann, C. R. Miller, Real-Time Magnetic Resonance Imaging of Bubble Behavior and Particle Velocity in Fluidized Beds, *Industrial & Engineering Chemistry Research* 57 (29) (2018) 9674–9682, doi:\let\@tempa\bibinfo@X@doi10.1021/acs.iecr.8b00932.
- [63] C. Boyce, A. Penn, M. Lehnert, K. Pruessmann, C. Miller, Effect of liquid bridging on bubbles injected into a fluidized bed: A magnetic resonance imaging study, *Powder Technology* 343 (2019) 813–820, doi:\let\@tempa\bibinfo@X@doi10.1016/j.powtec.2018.11.091.

**Declaration of interests**

The authors declare that they have no known competing financial interests or personal relationships that could have appeared to influence the work reported in this paper.

Journal Pre-proof